2014

# PRECISE CONTROL OF CARBON NANOTUBE MEMBRANE STRUCTURE FOR ENZYME MIMETIC CATALYSIS

Nicholas W. Linck
*University of Kentucky*, nwli222@uky.edu

STUDENT AGREEMENT:

I represent that my thesis or dissertation and abstract are my original work. Proper attribution has been given to all outside sources. I understand that I am solely responsible for obtaining any needed copyright permissions. I have obtained needed written permission statement(s) from the owner(s) of each third-party copyrighted matter to be included in my work, allowing electronic distribution (if such use is not permitted by the fair use doctrine) which will be submitted to UKnowledge as Additional File.

I hereby grant to The University of Kentucky and its agents the irrevocable, non-exclusive, and royalty-free license to archive and make accessible my work in whole or in part in all forms of media, now or hereafter known. I agree that the document mentioned above may be made available immediately for worldwide access unless an embargo applies.

I retain all other ownership rights to the copyright of my work. I also retain the right to use in future works (such as articles or books) all or part of my work. I understand that I am free to register the copyright to my work.

REVIEW, APPROVAL AND ACCEPTANCE

The document mentioned above has been reviewed and accepted by the student's advisor, on behalf of the advisory committee, and by the Director of Graduate Studies (DGS), on behalf of the program; we verify that this is the final, approved version of the student's thesis including all changes required by the advisory committee. The undersigned agree to abide by the statements above.

Nicholas W. Linck, Student

Dr. Bruce J Hinds, Major Professor

Dr. Fuqian Yang, Director of Graduate Studies

# PRECISE CONTROL OF CARBON NANOTUBE MEMBRANE STRUCTURE FOR ENZYME MIMETIC CATALYSIS

## Thesis

**A thesis submitted in partial fulfillment of the requirements for the degree of Master of Science in Materials Science and Engineering in the College of Engineering at the University of Kentucky**

**By Nicholas W. Linck**

**Lexington, KY**

**Director: Dr. Bruce J. Hinds, Professor of Materials Science and Engineering**

**Lexington, KY**

**2014**

## ABSTRACT OF THESIS

# PRECISE CONTROL OF CARBON NANOTUBE MEMBRANE STRUCTURE FOR ENZYME MIMETIC CATALYSIS

The ability to fabricate a charge-driven water pump is a crucial step toward mimicking the catalytic ability of natural enzyme systems. The first step towards making this water pump a reality is the ability to make a carbon nanotube (CNT) membrane with uniform, 0.8 nm pore diameter. Proposed in this work is a method for synthesizing these carbon nanotubes via VPI-5 zeolite templated, transition metal catalyzed pyrolysis. Using a membrane composed of these CNTs, it is possible to get water molecules to flow single file at a high flow rate, and to orient them in such a way that would maximize their ability to be catalyzed. Additionally, using the ability to plate a monolayer of precious metal catalyst molecules around the exit to the membrane, catalyst efficiency can be maximized by making every catalyst atom come into contact with a substrate molecule. In this work, we also demonstrate the ability to plate a monolayer of precious metal catalyst atoms onto an insulating, mesoporous, support material. By combining these two chemical processes, it is possible to mimic the catalytic efficiency of natural enzyme systems.

KEYWORDS: Carbon nanotube membrane, CNT Synthesis, Catalysis, VPI-5, Underpotential deposition

Nicholas W. Linck

14 July 2014

# PRECISE CONTROL OF CARBON NANOTUBE MEMBRANE STRUCTURE FOR ENZYME MIMETIC CATALYSIS

By

Nicholas W. Linck

Dr. Bruce J. Hinds

Dr. Fuqian Yang

14 July 2014

**Acknowledgements**

I would like to acknowledge my advisor Dr. Bruce J. Hinds for his support of my graduate study and guidance in my research work. I also would like to thank DARPA and DOE KY EPSCOR for funding the work presented in this dissertation.

I also would like to thank my committee members, Dr. Rodney Andrews and Dr. Dibakar Bhattacharyya, for their interest in my research and advice.

I would also like to thank my labmates, Zhiqiang Chen, Tao Chen, Dr. Guarav Gulati, and Dr. Rupam Sarma for their assistance and training with all equipment and experiments.

# Table of Contents

## List of Tables

## List of Figures

# Ch. 1: Introduction

A shortage of fresh water and the relative lack of clean, renewable energy are two large scale problems that can be improved by utilizing breakthroughs in membrane technology. Water is the most important resource needed to sustain human civilization due to the pivotal role it plays in agriculture and industry. While water is plentiful, covering roughly 70% of the surface of the earth, very little of it (~3%) is the fresh water that is useable for human consumption and agriculture, the vast majority of which is inaccessible due to being frozen in the polar ice caps[68]. This makes the ability to desalinate salt water paramount to advancing the human race. Reverse osmosis is currently the most widely used method to desalinate water, but it suffers from having high energy and capital costs. This is due to the exceptionally high surface area that is required in order to get water to move through the thick membrane layer and the high amount of energy needed to sustain the flow needed to reduce concentration polarization. Ideally, the membrane would have pores that are small enough to exclude salt ions, while allowing water molecules to rapidly flow single-file through the membrane, much like the aquaporin protein channels found in cell walls.

Due to the eventual depletion of nonrenewable energy sources, the need for clean, renewable energy sources is one of the most important issues facing humanity. Hydrogen energy is one of the viable candidates to replace fossil fuels as an energy source. One of the production processes for hydrogen involves the electrolysis of water in polymer electrolyte membrane fuel cells (PEMs). PEMs are becoming increasingly available in the commercial sector, due to their relative simplicity compared to other production methods as well as their ability to accept a wide variety of voltage inputs, making them ideal for use for solar photovoltaics (PV). PEMs work by electrochemically splitting water, producing hydrogen ($H_2$) at the cathode and oxygen ($O_2$) at the anode, while conducting protons through a polymer electrolyte from the anode to

the cathode. It is then possible to use these gases as a way to store energy for future use. The major drawback to PEMs is the high cost of the device brought about due to the precious metal catalyst required to split water.

The ability to get water molecules to flow single file through a membrane at a high flux rate is a crucial step toward creating a membrane that can mimic the natural catalysis of an enzyme. Using a CNT membrane with 8Å pore diameter and adding charges along the pore in a distribution that mimics that of biological aquaporins, a molecular water pump can theoretically be fabricated[59]. This water pump, simulated by Fang, et al, has shown an average net flux under a 1atm external pressure that is comparable to that of aquaporin-1.

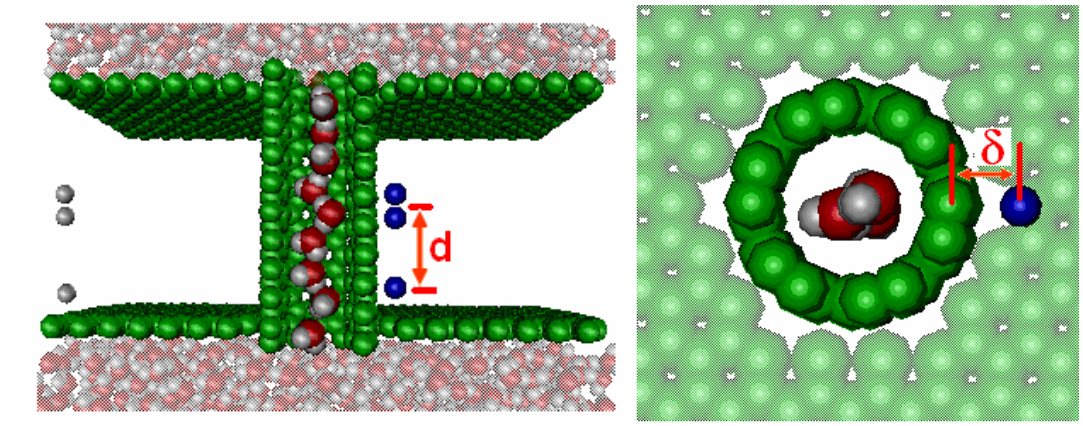


**Figure 1-1:** Molecular dynamics simulation of a theoretical charge-driven molecular water pump, where water molecules flow single-file through the hydrophobic core of a carbon nanotube. Image reproduced from Fang, et al[59]

Using this ability, it is possible to lay out the charges in a manner that mimics an enzyme's ability to orient the water molecule in a way that is ideal for catalysis. A monolayer of catalyst atoms can then be placed at the exit of the CNT membrane, allowing for maximum catalytic efficiency[60]. Using these principles, it is theoretically possible to reach the catalytic efficiency that is demonstrated by natural enzyme systems.

### 1.1 Water Desalination

Numerous methods have been used in the past to try to achieve maximum levels of desalination efficiency, including distillation[57] and reverse osmosis[58]. In the past decade or so, reverse osmosis (RO) systems have become one of the most popular, due to their relatively low energy cost compared to the more traditional distillation system. RO is a method of water purification that involves applying enough pressure to overcome the osmotic pressure and forcing the water through a semipermeable membrane, leaving the solute molecules (or ions) behind. A schematic of a typical reverse osmosis unit is shown in Figure 1-2.

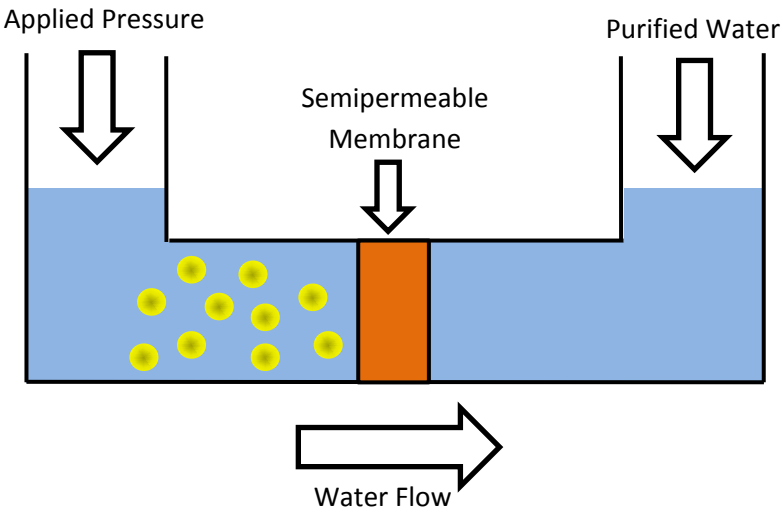


**Figure 1-2:** Schematic diagram of a general reverse osmosis (RO) system, where a pressure greater than the osmotic pressure of the fluid is applied, forcing water through a semipermeable membrane.

An ideal water desalination membrane would exhibit maximum flux and salt rejection, while simultaneously being mechanically robust and inexpensive. The desalination process would also minimize the energy required to achieve these levels of efficiency.

### 1.1.1 Carbon Nanotube Membranes

Since they were first described in 1991 by Ijima[17], carbon nanotubes (CNTs) have been heavily studied due to their extraordinary mechanical, electrical, optical, and thermal properties. Previous work by the Hinds' group has shown that semipermeable membranes can be produced using aligned carbon nanotubes as the pore structure, as shown in Figure 1-3[1].

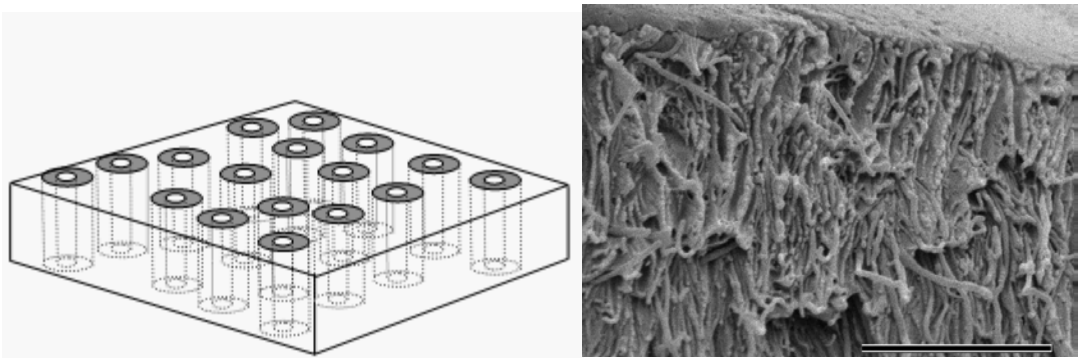

**Figure 1-3:** Schematic of the carbon nanotube membrane structure, with a polymer matrix surrounding the CNTs (left) and SEM micrograph of the cleaved edge of the CNT membrane, scale bar 2.5 µm (right). Images reproduced from Hinds, et al[1].

CNT membranes have numerous properties that make them superior to conventional membrane materials. Due to the hydrophobic, atomically flat core of the carbon nanotubes, CNT membranes show fluid flow up to four orders of magnitude higher than conventional membranes[60]. Also, the tips of the CNTs can be functionalized with a variety of different functional groups, giving rise to a large range of applications, including catalysis, water purification, and chemical separations.

### 1.1.2 Optimal CNT Membrane Diameter

Previous study by Corry[2] of the energetics of water and ion transport examined a range of differently sized carbon nanotubes for their viability for use in water desalination membranes. This study showed, through molecular dynamics simulations that membranes comprising of carbon nanotubes with diameters smaller than one nanometer can provide efficient means of

water desalination in a reverse osmosis system. Since the pores of these membranes are so narrow, they provide high levels of salt rejection while still allowing water molecules to flow single file through the cores of the carbon nanotubes, therefore keeping the high flux that is demonstrated by carbon nanotube membranes.

By testing CNTs of varying chiralities, It was determined through these calculations that the optimum carbon nanotubes for these membranes are of the (6,6) armchair chirality (d~0.8nm), as shown in Figure 1-4.

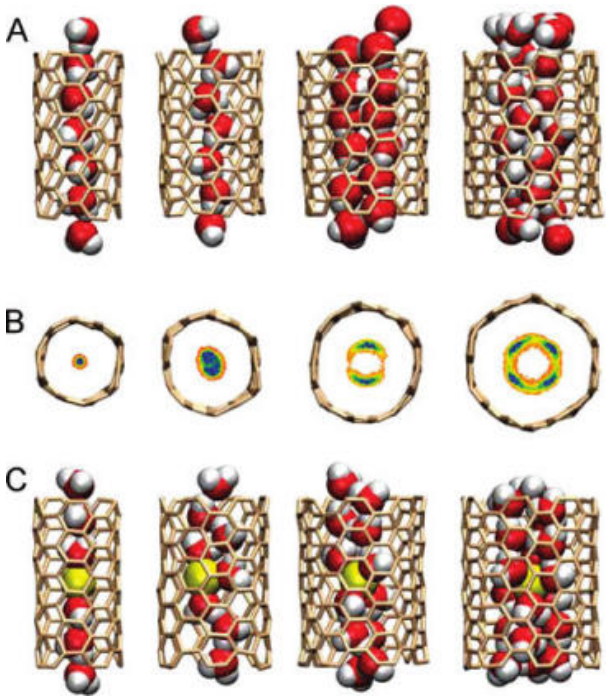


**Figure 1-4:** Model of CNTs made by Corry, et al, of (5,5), (6,6), (7,7), and (8,8) chiralities from left to right, showing (A) Configuration of water in CNT, (B) Top view of CNT showing structure of water in the pore, and (C) Location and hydration structure of $Na^+$ ions in the CNT pore. Images reproduced from Corry[2].

If the CNTs are any smaller than this, the membrane will be impermeable to both the salt ions as well as the water molecules in the system, thus not being useful for a desalination unit. Conversely, if the CNT is any larger than (6,6), the salt rejection will greatly decrease. Thus, the

ideal membrane in this case is composed of (6,6) armchair CNTs, which allow water molecules to flow single file through the pores at a high flow rate while achieving the maximum salt rejection.

### 1.1.3 Transition Metal Catalysts

Although there are multiple ways to synthesize carbon nanotubes, such as laser discharge and electric arc discharge, the most commonly used method is via chemical vapor deposition (CVD), due to its ability to work on a large scale at relatively low costs[75]. Metal nanoparticle catalysts play a crucial role in the synthesis of carbon nanotubes via CVD. Although many different metal catalysts, such as Au, Pt, Mo, and Cu have been used in the past, the most active and most commonly used are Fe, Co, Ni, and their alloys[76].

Transition metals, such as Fe, Co, Ni, and their alloys catalyze the decomposition of the carbon precursors, leading to supersaturated carbon precipitate and the formation of carbon nanotubes according to the vapor-liquid-solid (VLS) theory[74]. The type of transition metal catalyst as well as the support material can have a great effect on the chirality of the CNTs[77] as well as their diameter. The diameter of the carbon nanotube that is formed from this catalyzed CVD process is primarily controlled by the size of the nanoparticle catalyst, as shown in Figure 1-5[3]. Due to the difficulty in constraining the size of nanoparticles to sub-nanometer diameters, some kind of template support is necessary to create a stable, consistent catalyst for this synthesis.

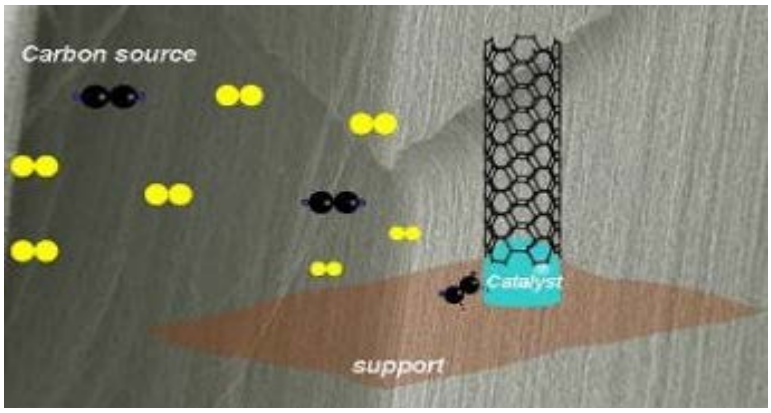


**Figure 1-5:** General diagram of CNT synthesis via supported transition metal catalyzed CVD. Image reproduced from Magrez, et al[3]

### 1.1.4 Zeolite Templated CNT Synthesis

Much research has gone into controlling the diameter of CNTs by growing them on zeolite templates. The first known instance of this was by Lucas et al. in 1996[43], using Y-type zeolite as the template with a cobalt catalyst support. Similar zeolite supported, transition metal catalyzed synthesis has since been reported numerous times[43-52] using various zeolites as the support. Many of these continued on with the common Y-type zeolite[47,48]. In other cases, ZSM-5 and MCM-41[49] as well as Silicate-1[52] have also been used as the template. For the purposes of making the diameter of nanotube needed for useful water desalination, the most relevant zeolite template that has been used before is AlPO4-5. This zeolite has been used to fabricate the smallest nanotube that has yet been reported, as shown in Figure 1-6[4].

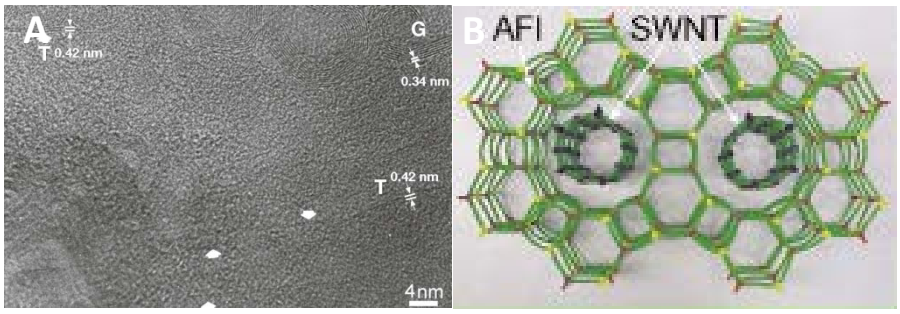


**Figure 1-6:** (A) TEM micrograph of ~0.4 nm carbon nanotubes that have been previously synthesized and (B) diagram of CNT's synthesized within pores of $AlPO_4$-5 zeolite. Images reproduced from Tang, et al[4].

The process involving the aluminophosphate zeolite differs from other templated CNT syntheses by synthesizing the CNT on the inside of the zeolite pore, rather than on the outer surface of the structure. This causes the CNT diameter to be more consistent by confining it more strictly to the desired diameter. Using AlPO4-5 zeolite, CNTs with diameters as small as 4Å have previously been fabricated[4].

### 1.1.5 VPI-5 Zeolite

Since its discovery by Davis in 1988[5], Virginia Polytechnic Institute number 5 (VPI-5) molecular sieve has studied intently. Everything from its synthesis[53] to its structural, and physiochemical characteristics have been researched over the past decades. VPI-5 is special as it is the first zeolite structure with pores larger than 10Å in diameter. It is similar in structure to the AlPO4-5 zeolite that was used by Zhai to fabricate the smallest nanotube, but with a ring structure containing 18 T-sites (~12Å pore), rather than the more common 12 T-sites (~8Å pore) as shown in Figure 1-7.

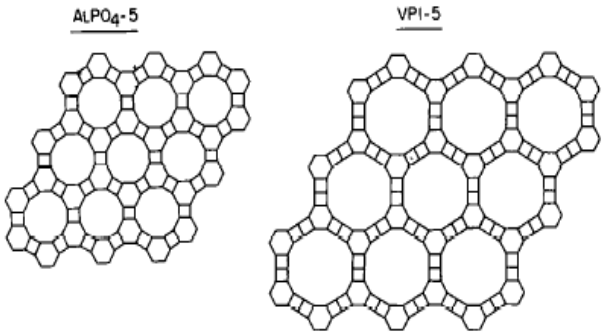


**Figure 1-7:** A comparison of the framework [100] projections of the 18 T-site VPI-5 and the 12 T-site $AlPO_4$-5. Images reproduced from Davis, et al[5]

In 1996, the synthesis procedure was optimized by Campi, et al[6], producing a procedure that would provide maximum VPI-5 yield. We hypothesize that, using a similar technique to that of

Zhai and using VPI-5 as the zeolite template, we can fabricate single-walled carbon nanotubes of 8Å diameter that would be ideal for use in a water desalination carbon nanotube membrane.

## 1.2 Monolayer Plating

### 1.2.1 PEM Water Electrolysis

Polymer electrolyte membrane (PEM) fuel cells are a developing industry in the fields of stationary and portable energy storage. They operate on the use of electrical energy to split water into hydrogen ($H_2$) and oxygen ($O_2$) gases via the following reaction:

$$2H_2O \longrightarrow 2H_2 + O_2$$

This process has the advantages of being able to operate at low temperatures and high current densities, giving them the ability to reduce operational costs when combined with other energy sources, such as wind or solar[67]. PEM electrolysis allows the electrical energy produced from sources with intermittent output to be converted to chemical energy and stored for use when output is low (i.e. when wind isn't blowing or when the when the sun isn't shining).

PEM water electrolyzers operate in an electrochemical cell where two water molecules are split at the anode into oxygen gas and four protons. While the two electrodes are electrically insulated from one another, the protons then migrate through a solid polymer electrolyte, and are converted into hydrogen gas at the cathode. A schematic of this process is shown in Figure 1-8.

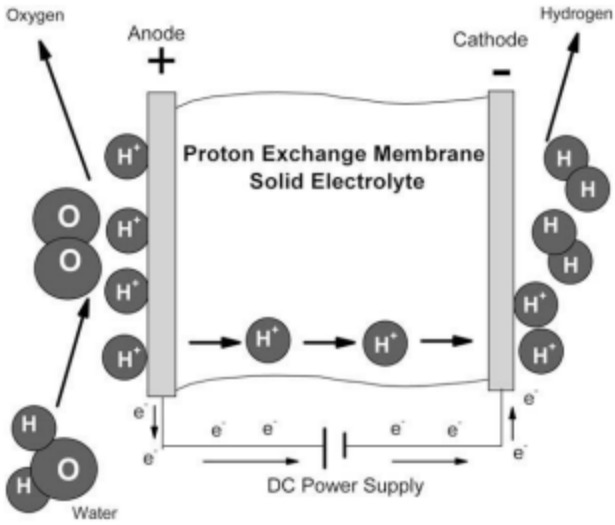


**Figure 1-8:** A schematic diagram of a general PEM fuel cell, showing water molecules being split into oxygen gas and protons at the anode and proton migration to the cathode.

As this reaction is not thermodynamically favorable, precious metal catalysts are necessary to minimize the amount of energy required to make it work.

### 1.2.2 Precious Metal Catalysts

Precious metals, such as platinum, palladium, and iridium are commonly used as catalysts for a number of different reactions. The most common of which is in automobile catalytic converters, which catalyze the oxidation of carbon monoxide (CO) and unburned hydrocarbons (CxHy) into carbon dioxide and water, as well as the reduction of NOx, shown below.

$$2CO + O_2 \longrightarrow 2CO_2$$

$$C_xH_{2x+x} + [(3x+1)/2]O_2 \longrightarrow xCO_2 + (x+1)H_2O$$

$$2NOx \longrightarrow xO_2 + N_2$$

The high cost of catalytic converters, beyond being an economic issue, also causes the issue of theft due to the high price of platinum that can be obtained from

They are also used to catalyze the electrooxidation of methanol in direct methanol fuel cells[70], the hydrogenation of unsaturated hydrocarbons[71], and the decomposition of hydrogen peroxide[72].

Multiple different metals, such as platinum and palladium[38] as well various alloys[61] have been used to catalyze the hydrogen evolution reaction (HER) of water electrolysis in the past. At the other end of the reaction, where the oxygen evolution reaction (OER) takes place, iridium[62] and ruthenium as well as oxides of the two[64, 63] are commonly used as the catalyst. Precious metals are commonly needed due to their high catalytic activity for their respective reactions as well as their high corrosion resistance in acidic media[38]. Currently, the state-of-the-art technology for minimizing the cost of these devices is through the use of precious metal nanoparticles supported on a highly porous substrate, such as mesoporous carbon[19]. While this currently provides the most efficient catalyst to date, the use of nanoparticles still leaves only about 30% of the catalyst atoms on the surface of the particle where it is available for catalysis. An ideal case for catalytic efficiency would be a monolayer of the precious metal supported on a high surface area, inexpensive substrate.

### 1.2.3 Underpotential Deposition

The process of underpotential deposition (UPD) happens when metal atoms are more attracted to a foreign substrate than to atoms of their own kind. This process is commonly used to deposit a monolayer or submonolayer of metal atoms (such as Cu or Ag) at a potential that is more

positive than the Nernst potential for bulk deposition[42]. This process has been demonstrated to work on a variety of conductive surfaces such as Au(111)[40] and nanoporous gold (npAu)[41]. A general schematic of the process is shown in Figure 1-9.

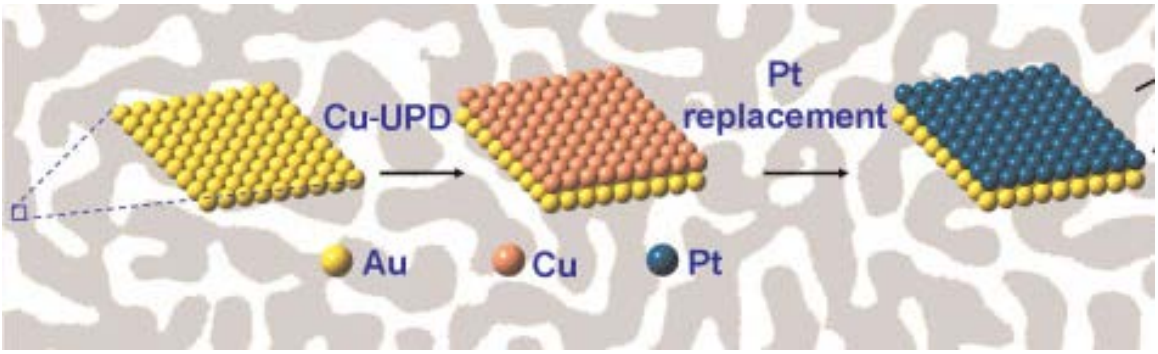


**Figure 1-9:** General schematic of copper monolayer underpotential deposition followed by redox replacement of platinum to produce a monolayer of platinum on surface of the substrate, reproduced from Wang, et al[18].

It has also been shown to work on nonmetal substrates such as conductive polymers[36] and carbon nanotube membranes[4].This process has also shown the ability to plate a monolayer of precious metal onto the substrate by monotonically replacing the copper atoms. During this process, the Cu monolayer is oxidized by more noble cations (i.e. $Pt^{4+}$, $Pd^{2+}$, $Ir^{3+}$)[66]. The overall process follows the redox reactions, wherein copper ions are first reduced to copper metal monolayer, and then is oxidized by platinum ions to produce a platinum metal monolayer and copper ions.

$$Cu^{2+} + 2e^{-} \longrightarrow Cu°$$

$$Pt^{4+} + Cu° + 2e^{-} \longrightarrow Pt° + Cu^{2+}$$

Previous work has only demonstrated this process to work on conductive substrates. We hypothesize that this technique can be used to plate a monolayer of catalyst atoms on the surface of a nonconductive material by first coating the substrate with a thin, gold film, thus lowering the cost of the catalyst by minimizing the amount of precious metal used.

### 1.3 Challenges

The key challenge to the project is the ability to synthesize single walled carbon nanotubes of consistent diameter. Previous research (as well as this work) shows encouraging signs that CNTs can be formed by pyrolyzing 1-pyrenebutyric acid that has been adsorbed into the pores of VPI-5 zeolite based on Raman results, but low CNT yield and high quantities of amorphous carbon formed during the process make confirming these results with TEM a daunting task.

The synthesis of CNTs by this method faces two large challenges. The primary challenge of this procedure is getting the carbon source and catalyst loaded into the pores of the zeolite. During the process described by Zhai[4], the organic template used in the zeolite synthesis becomes trapped within the pores during synthesis. This means that the process can be carried out simply by pyrolyzing the zeolite after synthesis. Since the organic template does not stay in the pores during the synthesis of VPI-5, the carbon precursor must be loaded into the pore after the fact. This gives rise to the second major challenge involved in this synthesis. Since the pores of VPI-5 show hydrophilic behavior, the carbon precursor must also have a hydrophilic group such as a hydroxyl or a carboxylic acid group attached to it in order to get adsorbed into the pores. This creates an additional issue, since VPI-5 decomposes at high temperatures in the presence of water[6]. If there is too much oxygen in the carbon precursor, the pyrolysis will produce water at high temperatures, thus destroying the zeolite template. A thermodynamic study was used to determine the optimal carbon precursor for this process, using the criteria that it must produce graphitic carbon in high quantities and minimize the amount of water produced in the reaction.

### 1.4 Summary of Key Goals

The ability to fabricate a charge-driven water pump, where molecules flow single file through the pores of a carbon nanotube (CNT) membrane is a crucial step toward mimicking the catalytic behavior of natural enzymes.

The first key component to fabricating such a device is the ability to synthesize CNTs with a uniform diameter of 0.8 nm. In this work, it is proposed that this goal can be accomplished by pyrolyzing a carbon precursor within the pores of VPI-5 zeolite. Once this is accomplished, the synthesized CNTs can be fabricated into a membrane. This will provide an ideal membrane for water desalination via reverse osmosis.

The second key component to mimicking the catalytic behavior of natural enzyme systems is the ability to place catalyst atoms on the pore exits of the membrane. It is proposed through this work that this can be accomplished using the underpotential deposition and redox replacement method to plate a monolayer of platinum atoms on the surface of the membrane. Since water molecules in this membrane will flow single-file through the CNT pores, each molecule will flow through the membrane at a high rate and come into contact with the catalyst at the exit, providing catalytic efficiency that approaches that of natural enzymes.

# Chapter 2: Zeolite Templated Synthesis of Carbon Nanotubes for Precise Diameter Control

## 2.1 Introduction

Since they were first described in 1991[17], carbon nanotubes (CNTs) have been extensively researched due to their exceptional mechanical, thermal, and electrical properties. Carbon nanotubes can also be aligned in such a way as to create a semipermeable membrane. These membranes composed of aligned CNTs exhibit fluid flow that is 4-5 orders of magnitude faster than conventional flow models predict. This high flow is due to the atomically flat, hydrophobic core of the carbon nanotubes[1]. Molecular dynamics simulations by Corry et al[2] show that (6,6) armchair CNTs make the optimal pores for water desalination in a CNT membrane by preventing salt ions from entering the membrane while allowing water molecules to flow single-file through the CNT core.

Prior research has demonstrated the ability to synthesize ultrafine carbon nanotubes within highly porous, rigid substrates (such as anodic alumina) via template carbonization[15]. This process involves exposing the template film to a carbon source at a high temperature in the absence of oxygen. This pyrolysis technique has also been reported on various mesoporous materials such as MCM-41. This technique has been used using many different carbon sources, such as sugars and other organics[16].

Previous research by Zhai et al, has demonstrated the ability to synthesize single-walled carbon nanotubes of 4Å diameter by pyrolyzing tripropylamine (TPA) within the pores of $AlPO_4$-5 zeolite[4]. This is a relatively easy procedure, as the TPA is the compound used to template the zeolite and is trapped within the pores during the synthesis. To date, these are the smallest

diameter SWNCT that have been synthesized. This method is able to consistently produce 4Å SWCNTs due to the crystalline structure and precisely controlled pore sizes of the zeolite.

Virginia Polytechnic Institute number 5 (VPI-5) molecular sieve is an aluminophosphate zeolite that is similar in structure and composition to $AlPO_4$-5 zeolite used by Zhai, but due to its 12-ring structure[5] has a uniform 1.2nm pore size. This larger pore size should allow the ability to serve as a suitable template for larger diameter SWCNT synthesis using a similar method as described by Tang. The challenge faced by VPI-5 is the fact that the synthesis of the zeolite does not trap the templating agent within the pores, so the carbon precursor for the synthesis must be loaded into the pores during a separate step.

Using the concepts outlined by Tang and Kyotani, et al. it has been hypothesized that 0.8nm diameter SWCNTs can be synthesized by adsorbing a carbon precursor into VPI-5 zeolite along with a transition metal catalyst. This loading procedure is then followed by pyrolysis of the sample within the template to produce nanotubes. These nanotubes can then be fabricated into an ideal CNT membrane for water desalination.

## 2.2 Methods

### 2.2.1 VPI-5 Synthesis

Since VPI-5 zeolite is not commercially available, it was synthesized using the procedure described by Anderson, et al[6]. Prior to synthesis, all equipment is cleaned with sodium hydroxide solution. Alumina slurry was made by adding 30 g Catapal B alumina (Boehmite) to 47.1 g deionized water and stirred for 10 minutes. 47.25 g of 81% phosphoric acid, diluted in 30.11 g $H_2O$ was added to the slurry at 3.5 $cm^3$/min. The rate at which the acid is added to the slurry is crucial to the synthesis procedure. If added too fast, the resulting hydrogel becomes very viscous and results in many impurities during crystallization. If added to slowly, the slurry

will not gel properly and will not form zeolite during crystallization. The mixture was then stirred using a propeller mixer for 5 minutes, followed by 2 hours of aging for the gel. After the aging process, 21.45 g of dipropylamine (DPA) was added to the gel at 3.5 $cm^3$/min (again, rate of addition is crucial), followed by a second, two-hour aging. The hydrogel was then transferred to a Teflon-lined, stainless steel autoclave (Parr) and placed in an oven to raise the hydrogel to the crystallization temperature of 130°C. After reaching the crystallization temperature, the autoclave and hydrogel were held at this temperature without stirring for 13 hours. After the crystallization process, the autoclave was quenched in water down to room temperature. The resulting mixture was then transferred to a beaker and the VPI-5 crystals were allowed to settle. The supernatant fluid was then removed from the crystals by decantation and the resulting powder was washed five times with DI water by agitation, followed by settling and decantation. Finally, the crystals were recovered by vacuum filtration and dried at room temperature in air overnight.

### 2.2.2 Catalyst

Multiple approaches were taken to getting the activated transition metal nanoparticle catalyst into the pores of the zeolite. Variations on the procedure include the transition metal that was used as the catalyst, the location of the metal nanoparticle relative to the carbon precursor, and the oxidation state of the catalyst.

Cobalt and iron were both used as catalysts for the synthesis of carbon nanotubes. Cobalt absorption into the pores of the VPI-5 was accomplished by soaking the crystals in a solution of cobalt chloride hexahydrate ($CoCl_2 \cdot 6H_2O$) for two hours. VPI-5 zeolite with $Fe^{3+}$ within the pores was synthesized via the procedure laid out by Prasad[9]. The same procedure was used to synthesize FeVPI-5 was the same as the procedure for synthesis of VPI-5 with $FeCl_3$ solution

added to the hydrogel mixture after the addition of the DPA and before the second aging period.

The location of the cobalt catalyst with respect to the carbon precursor was also varied in an attempt to improve the process. The first process involved adsorbing the cobalt into the zeolite and reducing it to Co nanoparticles prior to infiltrating the pores with the carbon precursor. The other method involved adsorbing the carbon precursor before the catalyst material, providing a type of "cap" on either end of the zeolite pore.

### 2.2.3 Carbon Precursor Determination

Two different compounds were considered as viable carbon sources for the synthesis of carbon nanotubes; fructose and 1-pyrenebutyric acid (PyBA). These carbon precursors were chosen based on two general criteria; that they must be hydrophilic in order to be adsorbed into the hydrophilic pores of the VPI-5 and that they must contain enough carbon atoms in their structure to be able to provide a significant amount of graphitic carbon when pyrolyzed. Based on these two criteria and general observations of the two compounds, either one could be regarded as a potential carbon source for this process.

Early synthesis attempts using fructose as the carbon source yielded poor results, and a thermodynamic study was undertaken to explain these results. This analysis was then repeated for PyBA in order to compare graphitic carbon production. It should be noted at this point that CNT growth uses a transition metal catalyst to form intermediate metal-carbides. However, these catalysts cannot perform thermodynamically unfavorable reactions and product analysis is critical. The ideally catalyzed reaction would proceed with the general form:

$$C_xH_yO_z \longrightarrow (x - \frac{y-2z}{4})C_{(s)} + \frac{y-2z}{4}CH_4 + zH_2O$$

And the two precursor compounds are shown below.

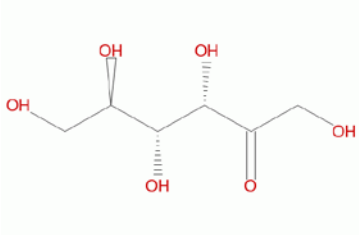


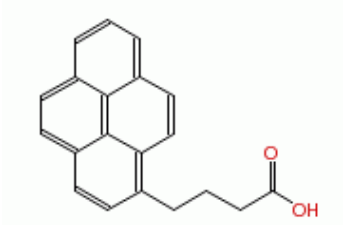


Fructose 1-pyrenebutyric acid

Upon searching the literature, the most common organic products of fructose were determined and the relevant thermodynamic quantities were found using the Standard Thermodynamic Properties of Chemical Substances table from the department of chemistry at the University of Indiana[12]. The results of this search are found in Table 2-1. Both sources listed other organics as products of the decomposition, but listing every conceivable product was not necessary to determine the proper carbon precursor.

**Table 2-1:** Most prominent organic products of fructose pyrolysis, along with relevant thermodynamic properties. Properties were found in the "Standard Thermodynamic Properties of Chemical Substances" table from the University of Indiana department of chemistry[6].

| Compound | ΔHf (kJ/mol) | S° (kJ/mol*K) | Reference |
|---|---|---|---|
| Benzene | 49.0 | 0.1733 | Higman et al[13] |
| Toluene | 12.0 | 0.2210 | Higman et al[13] |
| Phenol | -165.0 | 0.1440 | Higman et al[13] |
| Ethylbenzene | -12.5 | 0.2550 | Higman et al[13] |
| Styrene | 103.4 | 0.2380 | Higman et al[13] |
| Indene | 110.6 | 0.2153 | Higman et al[13] |
| Acetaldehyde | -166.2 | 0.2638 | Fagerson et al[14] |
| Acetone | -217.1 | 0.2953 | Fagerson et al[14] |
| Ethanol | -234.8 | 0.2816 | Fagerson et al[14] |
| Acetic Acid | -432.2 | 0.2835 | Fagerson et al[14] |
| Furan | -34.8 | 0.2672 | Fagerson et al[14] |

In order to quantify the graphitic carbon formed during the decomposition of fructose, it is necessary to determine the Gibb's free energy of each decomposition product forming. A

hypothetical reaction was devised for each product to determine the stoichiometry and additional products (e.g. $H_2O$, $CO_2$, and CO) that would be necessary for a full thermodynamic analysis. These reaction products are summarized in Table 2-2. It is worth noting at this point that for fructose, out of twelve decomposition reactions, only five have the stoichiometric ability to produce graphitic carbon.

**Table 2-2:** Balanced chemical reactions for the twelve main products of fructose decomposition. Note that only toluene, ethylbenzene, styrene, indene, and graphite reactions produce graphitic carbon.

| **Balanced Reactions (Oxygen Compounds)** | **Balanced Reactions (Non-Oxygen Compounds)** |
|---|---|
| Acetaldehyde Reaction | Benzene Reaction |
| $2\ C_6H_{12}O_6 \rightarrow 6\ C_2H_4O\ \ 3\ O_2$ | $2\ C_6H_{12}O_6 \rightarrow 2\ C_6H_6\ \ 6\ H_2O$ |
| Acetone Reaction | Toluene Reaction |
| $C_6H_{12}O_6 \rightarrow 2\ C_3H_6O\ \ 2\ O_2$ | $2\ C_6H_{12}O_6 \rightarrow C_7H_8\ \ 6\ H_2O\ \ 5\ C_{(s)}\ \ 2\ H_2$ |
| Ethanol Reaction | Ethylbenzene Reaction |
| $C_6H_{12}O_6 \rightarrow 2\ C_2H_6O\ \ 2\ CO_2$ | $2\ C_6H_{12}O_6 \rightarrow C_8H_8\ \ 6H_2O\ \ 4\ C_{(s)}\ \ H_2$ |
| Acetic Acid | Styrene Reaction |
| $C_6H_{12}O_6 \rightarrow 2\ C_2H_4O_2\ \ 2\ CO\ \ H_2\ \ H_2O$ | $2\ C_6H_{12}O_6 \rightarrow C_8H_8\ \ 6\ H_2O\ \ 4\ C_{(s)}\ \ 2\ H_2$ |
| Furan Reaction | Indene Reaction |
| $C_6H_{12}O_6 \rightarrow C_4H_4O\ \ 3\ H_2O\ \ 2\ CO_2\ \ H_2$ | $2\ C_6H_{12}O_6 \rightarrow C_9H_8\ \ 6\ H_2O\ \ 3\ C_{(s)}\ \ 2\ H_2$ |
| Phenol Reaction | Graphite Reaction |
| $C_6H_{12}O_6 \rightarrow C_6H_6O\ \ 3\ H_2O\ \ O_2$ | $C_6H_{12}O_6 \rightarrow 6\ C_{(s)}\ \ 6\ H_2O$ |

After the stoichiometry of these reactions was determined, the Gibb's free energy of each reaction ($\Delta G_r$) was calculated and plotted against temperature, using the following equations:

$$\Delta G_f = \Delta H_f - T\Delta S_f$$

$$\Delta G_r = \Sigma \Delta G_{f,products} - \Sigma \Delta G_{f,reactants}$$

Where $\Delta H_f$ is the standard enthalpy of formation, $\Delta S_f$ is the standard molar entropy of the compound and T is temperature. $\Delta H_f$ and $\Delta S_f$ for most of the compounds were found in the literature and are summarized in Table 2-1. $\Delta S_f$ for fructose could not be found in the literature, so it was assumed to be the same as that of glucose (since the difference between the two

compounds is minimal). The calculated Gibb's free energies were then used to determine if the formation of each product was thermodynamically favorable (and at what temperature).

1-pyrenebutyric acid was analyzed in a similar manner to fructose in order to compare their viabilities as carbon precursor options. Two assumptions were made for the PyBA model. First, it was assumed that the primary volatile organic products would be the same for PyBA as for fructose. Again, it is to be noted that analyzing every conceivable product is unnecessary. The second assumption is based on the fact that no literature values could be found for the $\Delta H_f$ and $\Delta S_f$ of PyBA. This was calculated by assuming that the $\Delta G_r$ was similar for the synthesis of PyBA from pyrene and butyric acid and the synthesis of 1-phenylbutyric acid from benene and butyric acid. The reactions are shown in Figure 2-1.

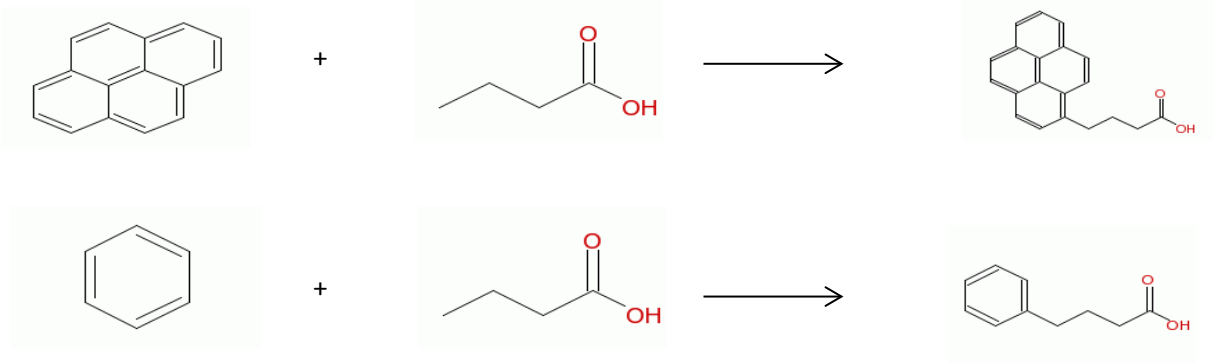


**Figure 2-1:** Two reactions that were assumed similar in order to determine thermodynamic properties of 1-pyrenebutyric acid.

The product summary for PyBA is shown in Table 2-3. Again, it is important to note that, due to the fact that PyBA contains 20 carbon atoms in the structure, none of the decomposition reactions can be balanced without forming graphitic carbon.

**Table 2-3:** Balanced chemical reactions for the twelve main products of 1-Pyrenebutyric acid decomposition. Note that, contrary to fructose decomposition, all twelve products produce graphitic carbon.

| **Balanced Reactions (Oxygen Compounds)** | | | | | **Balanced Reactions (Non-Oxygen Compounds)** | | | | | |
|---|---|---|---|---|---|---|---|---|---|---|
| Acetaldehyde Reaction | | | | | Benzene | | | | | |
| $C_{20}H_{16}O_2$ | → | 2 $C_2H_4O$ | 2 $CH_4$ | 14 C | $C_{20}H_{16}O_2$ | → | 2 $C_6H_6$ | $CH_4$ | $CO_2$ | 6 C |
| Acetone Reaction | | | | | Toluene | | | | | |
| $C_{20}H16O2$ | → | 2 $C_3H_6O$ | $CH_4$ | 13 C | $C_{20}H_{16}O_2$ | → | 2 $C_7H_8$ | $CO_2$ | 5 C | |
| Ethanol Reaction | | | | | Ethylbenzene | | | | | |
| $C_{20}H_{16}O_2$ | → | 2 $C_2H_6O$ | $CH_4$ | 15 C | $C_{20}H_{16}O_2$ | → | $C_8H_{10}$ | $2H_2O$ | $H_2$ | 12 C |
| Acetic Acid | | | | | Styrene | | | | | |
| $C_{20}H_{16}O_2$ | → | $C_2H_4O_2$ | 3 $CH_4$ | 15 C | $C_{20}H_{16}O_2$ | → | 2 $C_8H_8$ | $CO_2$ | 4 C | |
| Furan Reaction | | | | | Indene | | | | | |
| $C_{20}H_{16}O_2$ | → | 2 $C_4H_4O_2$ | 2 $CH_4$ | 10 C | $C_{20}H_{16}O_2$ | → | 2 $C_9H_8$ | $CO_2$ | C | |
| Phenol Reaction | | | | | Graphite | | | | | |
| $C_{20}H_{16}O_2$ | → | 2 $C_6H_6O$ | $CH_4$ | 7 C | $C_{20}H_{16}O_2$ | → | 17 C | 2 $H_2O$ | 3 $CH_4$ | |

The Gibb's free energies of these reactions were then plotted against temperature for both potential carbon precursors.

### 2.2.4 Carbon Precursor Adsorption

As described by the thermodynamic study, 1-pyrenebutyric acid (PyBA) was determined to be the carbon source that most adequately meets the necessary criteria that is required to synthesize carbon nanotubes via this process. Three different methods of absorption were attempted to get the PyBA into the pores of the zeolite and the best method was determined by percent graphitic carbon residue obtained from thermogravimetric analysis (TGA).

#### 2.2.4.1 Solution-based Adsorption

Prior to being adsorbed with carbon precursor, VPI-5 crystals were dried in a vacuum oven overnight. 50mg of VPI-5 was then immersed in a 10mM solution of 1-pyrenebutyric acid in acetone. The sample was then stirred in this solution for three hours. Crystals were then collected via vacuum filtration and dried in the vacuum oven overnight.

#### 2.2.4.2 Sublimation Infiltration (Mechanically Mixed)

50mg of VPI-5 crystals were first mechanically mixed with 10mg of PyBA by grinding together with a mortar and pestle. The mixture was then transferred to an alumina boat and placed inside a tube furnace. Vacuum was pulled inside the furnace and the temperature was raised from room temperature to 100°C at a rate of ~2°C/min. Sample was held at 100°C for 1 hour to purge out any water that may be trapped within the pores of the zeolite. Since PyBA sublimes at 150°C at low pressures, furnace was then ramped to 150°C at ~2°C/min and held at this temperature while maintaining vacuum for 4 hours. The mixture was then cooled to room temperature, washed with acetone, and dried overnight.

#### 2.2.4.3 Sublimation Infiltration (With Porous AAO Barrier)

10mg PyBA was placed at the bottom of an alumina boat. A piece of porous alumina (AAO) membrane was placed on top of the PyBA powder, and 50mg VPI-5 crystals was placed on top of the AAO membrane. Boat was then placed inside the tube furnace and vacuum was pulled on the sample. Temperature of the furnace was then raised to from room temperature to 100°C at a rate of 2°C/min and held at this temperature for 1 hour to remove any water from the zeolite. Temperature was then raised to 150°C at a rate of 2°C/min and held at this temperature under vacuum for 4 hours before being cooled back down to room temperature. VPI-5 was then removed from top of the AAO barrier.

### 2.2.5 Pyrolysis

A general overview of the pyrolysis procedure goes as such. A sample of VPI-5 loaded with catalyst nanoparticles and carbon precursor was put in an alumina boat that was subsequently placed in a tube furnace. The furnace was then attached to a double bubbler and purged with argon five times by alternately pulling vacuum and flowing argon gas in the furnace. The

temperature was then raised to 100°C and held at this temperature for 1 hour to purge out any water that may be trapped within the pores of the zeolite. After the water purge step, the temperature of the furnace was raised to the pyrolysis temperature at a rate of 10°C/min and held at that temperature for 1 hour before being cooled back down to room temperature. The appropriate temperature for pyrolysis was determined by treating the zeolite that was not loaded with cobalt or carbon precursor to various temperatures between 600 and 1000°C. XRD was then taken of the zeolite after this annealing to determine if the VPI-5 retained the pore structure necessary for carbon nanotube synthesis.

### 2.2.6 Post Pyrolysis Treatment

After pyrolysis, the zeolite structure was dissolved away by immersing in the sample in 10% hydrochloric acid (HCl) and stirring for 1 hour.

As will be discussed in the results and discussion section, Raman spectroscopy indicated that carbon nanotubes ~0.8nm in diameter were present in multiple samples. Due to large amounts of amorphous carbon that was also present in the samples, transmission electron microscopy (TEM) was not able to confirm the presence of these CNTs via direct imaging. Several different post-pyrolysis treatments were applied to the samples in order to improve the chances of seeing CNTs using TEM.

Based on the principle that hydrogen peroxide ($H_2O_2$) oxidizes amorphous carbon at a higher rate than carbon nanotubes and will not damage the zeolite structure[10], it was proposed that the concentration of CNTs relative to amorphous carbon could be improved by treating the pyrolyzed carbon product with $H_2O_2$ prior to dissolving the zeolite in HCl to remove any carbon product that was formed on the outside of the zeolite and leave the CNTs that were formed within the pores intact.

Another tactic for making CNTs more visible using TEM was to add Triton surfactant to the liquid mixture during ultrasonication.

### 2.2.7 Characterization

#### 2.2.7.1 X-Ray Diffraction (XRD)

A Siemens D500 Powder X-ray diffractometer (XRD), operating with Cu Kα radiation (λ=1.5408Å) was used to characterize the synthesized VPI-5. A 2θ scan from 4° to 40° at a rate of 1.0° per minute was used.

#### 2.2.7.2 Scanning Electron Microscopy (SEM)

Scanning electron microscopy was used to image the VPI-5 crystals and was carried out on an S-4300 Hitachi microscope. All zeolite samples were sputter coated with gold prior to analysis.

#### 2.2.7.3 Micro-Raman Spectroscopy

Raman spectroscopy was used to characterize carbon nanotubes. Analysis was carried out using a dispersive Micro-Raman spectrometer from Thermo Scientific using 780nm laser excitation. Also used was a Renishaw inVia Raman Microscope with a red laser (633 nm) and a 150 W maximum power.

#### 2.2.7.4 Thermogravimetric Analysis (TGA)

TGA was used to determine graphitic carbon content of the zeolite after various absorption processes. TGA was run on a NETZSCH STA449C thermal instrument. The sample was heated from room temperature to 1000°C at a rate of 10°C/min under flowing nitrogen (20 $cm^3$/min), followed by a carbon burn at 1000°C with flowing air for 30 minutes. The graphitic carbon content was determined by the weight loss associated with this final carbon burn.

## 2.3 Results and Discussion

### 2.3.1 Synthesis of VPI-5

Following the optimized procedure by Anderson, et al[5], VPI-5 was synthesized and characterized by x-ray diffraction (XRD) and scanning electron microscopy (SEM). Major diffraction peak for [100], representing the largest d-spacing in the structure, verifies that the pore structure we need for our synthesis is present, as shown in Figure 2-2. Subsequent XRD after various annealing temperatures confirm that zeolite retains its pore structure at pyrolysis temperature, provided the sample was thoroughly dried prior to being raised to this temperature.

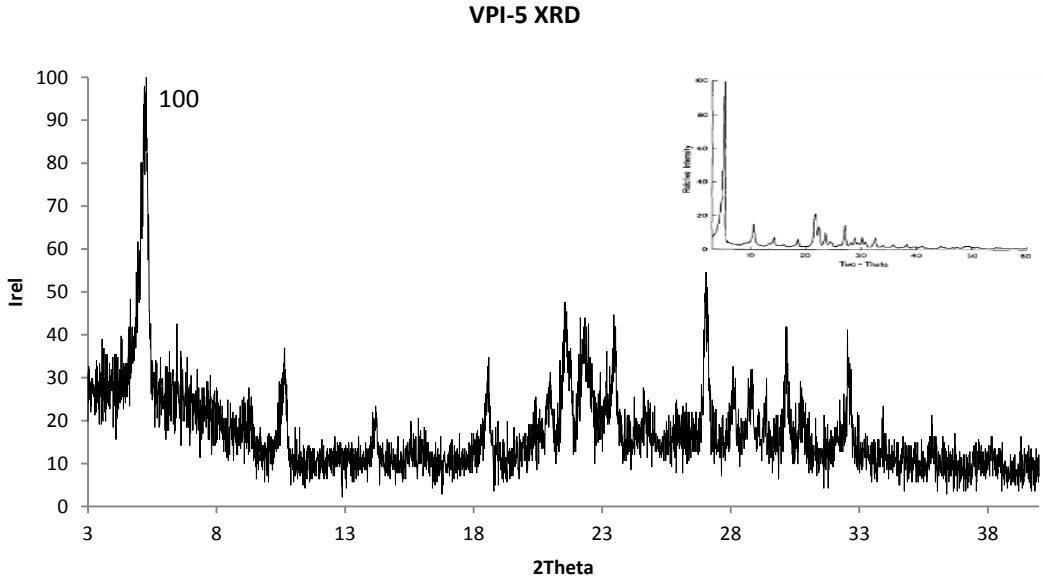


**Figure 2-2:** XRD plot of synthesized VPI-5, highlighting [100] peak. Crystalline data for VPI-5: a = b = 18.975 Å, c = 8.104 Å α = β = 90°, γ = 120°. Inset: reference VPI-5 XRD pattern[5]

SEM was also used to characterize VPI-5 by directly imaging the crystal to determine structure and estimate their length. As seen in Figure 2-3, the long, needle-like crystal structure that is characteristic of VPI-5 is clearly present.

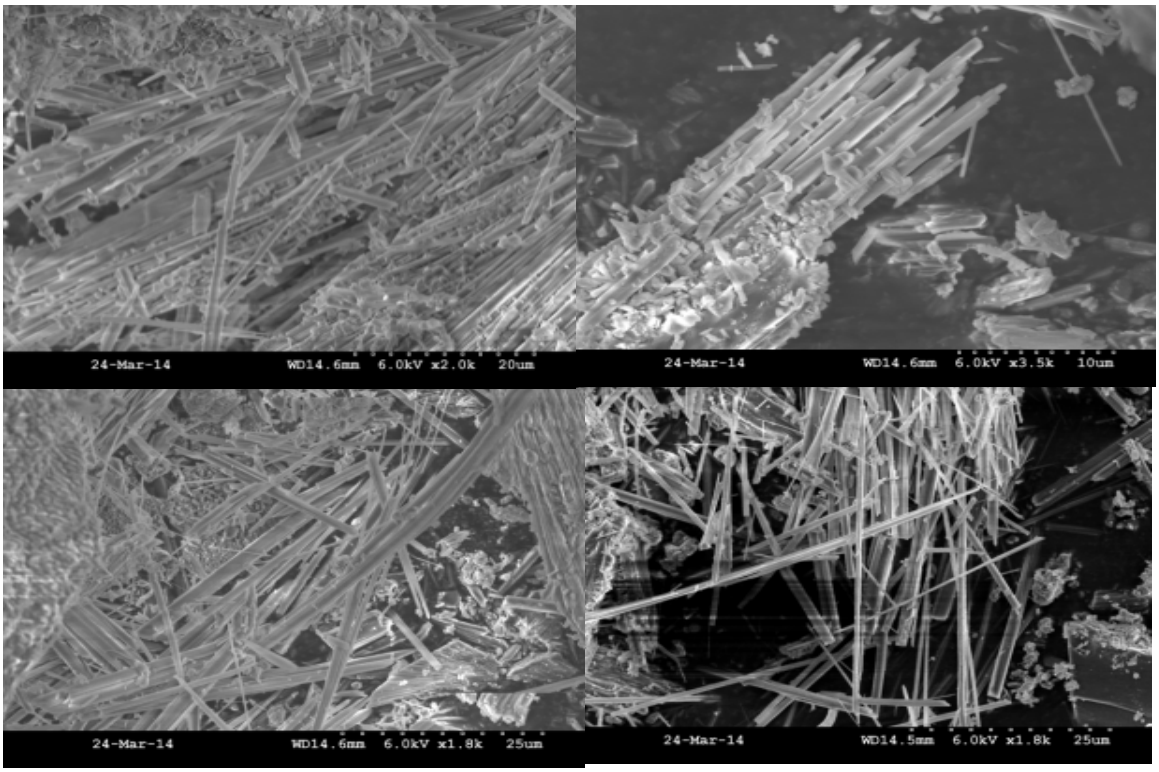


**Figure 2-3:** SEM images of VPI-5 crystals, confirming long, needle-like structure.

### 2.3.2 Thermodynamic Study of Carbon Precursors

#### 2.3.2.1 Fructose

After all potential decomposition reactions were balanced, the Gibbs' free energy of formation was calculated for all products, including numerous small molecules, such as carbon dioxide, water, and methane, using the equations listed previously along with literature values for enthalpy of formations and standard molar entropy. Since the CNT synthesis reaction involves temperatures up to about 1250 K, the temperature was varied from room temperature to 1250 K. the free energies of the oxygen-containing and non-oxygen –containing products are shown in Tables 2-4 and 2-5 respectively.

**Table 2-4:** Calculated Gibbs' free energies of formation for all oxygen containing products of fructose decomposistion.

| | Acetaldehyde | Acetone | Ethanol | Acetic Acid | Furan | Fructose | Carbon Dioxide | Water | Oxygen | Phenol | Carbon Monoxide |
|---|---|---|---|---|---|---|---|---|---|---|---|
| **T (K)** | **ΔGf** | **ΔGf** | **ΔGf** | **ΔGf** | **ΔGf** | **ΔGf** | **ΔGf** | **ΔGf** | **ΔGf** | **ΔGf** | **ΔGf** |
| **300** | -245.34 | -305.69 | -319.28 | -512.36 | -114.96 | -1333.7600 | -457.4 | -298.2 | -61.5 | -208.2 | -169.6 |
| **350** | -258.53 | -320.455 | -333.36 | -525.72 | -128.32 | -1344.2200 | -468.05 | -307.6 | -71.75 | -215.4 | -179.45 |
| **400** | -271.72 | -335.22 | -347.44 | -539.08 | -141.68 | -1354.6800 | -478.7 | -317 | -82 | -222.6 | -189.3 |
| **450** | -284.91 | -349.985 | -361.52 | -552.44 | -155.04 | -1365.1400 | -489.35 | -326.4 | -92.25 | -229.8 | -199.15 |
| **500** | -298.1 | -364.75 | -375.6 | -565.8 | -168.4 | -1375.6000 | -500 | -335.8 | -102.5 | -237 | -209 |
| **550** | -311.29 | -379.515 | -389.68 | -579.16 | -181.76 | -1386.0600 | -510.65 | -345.2 | -112.75 | -244.2 | -218.85 |
| **600** | -324.48 | -394.28 | -403.76 | -592.52 | -195.12 | -1396.5200 | -521.3 | -354.6 | -123 | -251.4 | -228.7 |
| **650** | -337.67 | -409.045 | -417.84 | -605.88 | -208.48 | -1406.9800 | -531.95 | -364 | -133.25 | -258.6 | -238.55 |
| **700** | -350.86 | -423.81 | -431.92 | -619.24 | -221.84 | -1417.4400 | -542.6 | -373.4 | -143.5 | -265.8 | -248.4 |
| **750** | -364.05 | -438.575 | -446 | -632.6 | -235.2 | -1427.9000 | -553.25 | -382.8 | -153.75 | -273 | -258.25 |
| **800** | -377.24 | -453.34 | -460.08 | -645.96 | -248.56 | -1438.3600 | -563.9 | -392.2 | -164 | -280.2 | -268.1 |
| **850** | -390.43 | -468.105 | -474.16 | -659.32 | -261.92 | -1448.8200 | -574.55 | -401.6 | -174.25 | -287.4 | -277.95 |
| **900** | -403.62 | -482.87 | -488.24 | -672.68 | -275.28 | -1459.2800 | -585.2 | -411 | -184.5 | -294.6 | -287.8 |
| **950** | -416.81 | -497.635 | -502.32 | -686.04 | -288.64 | -1469.7400 | -595.85 | -420.4 | -194.75 | -301.8 | -297.65 |
| **1000** | -430 | -512.4 | -516.4 | -699.4 | -302 | -1480.2000 | -606.5 | -429.8 | -205 | -309 | -307.5 |
| **1050** | -443.19 | -527.165 | -530.48 | -712.76 | -315.36 | -1490.6600 | -617.15 | -439.2 | -215.25 | -316.2 | -317.35 |
| **1100** | -456.38 | -541.93 | -544.56 | -726.12 | -328.72 | -1501.1200 | -627.8 | -448.6 | -225.5 | -323.4 | -327.2 |
| **1150** | -469.57 | -556.695 | -558.64 | -739.48 | -342.08 | -1511.5800 | -638.45 | -458 | -235.75 | -330.6 | -337.05 |
| **1200** | -482.76 | -571.46 | -572.72 | -752.84 | -355.44 | -1522.0400 | -649.1 | -467.4 | -246 | -337.8 | -346.9 |
| **1250** | -495.95 | -586.225 | -586.8 | -766.2 | -368.8 | -1532.5000 | -659.75 | -476.8 | -256.25 | -345 | -356.75 |

**Table 2-5:** Calculated Gibbs' free energies of formation for all non-oxygen-containing products of fructose decomposition.

| | Benzene | Toluene | Ethylbenzene | Styrene | Indene | Graphite | Hydrogen | Methane |
|---|---|---|---|---|---|---|---|---|
| T (K) | ΔGf | ΔGf | ΔGf | ΔGf | ΔGf | ΔGf | ΔGf | ΔGf |
| **300** | -4.19 | -54.3 | -64 | 32 | 46.01 | -1.71 | -39 | -130.49 |
| **350** | -13.055 | -65.35 | -76.75 | 20.1 | 35.245 | -1.995 | -45.5 | -139.805 |
| **400** | -21.92 | -76.4 | -89.5 | 8.2 | 24.48 | -2.28 | -52 | -149.12 |
| **450** | -30.785 | -87.45 | -102.25 | -3.7 | 13.715 | -2.565 | -58.5 | -158.435 |
| **500** | -39.65 | -98.5 | -115 | -15.6 | 2.95 | -2.85 | -65 | -167.75 |
| **550** | -48.515 | -109.55 | -127.75 | -27.5 | -7.815 | -3.135 | -71.5 | -177.065 |
| **600** | -57.38 | -120.6 | -140.5 | -39.4 | -18.58 | -3.42 | -78 | -186.38 |
| **650** | -66.245 | -131.65 | -153.25 | -51.3 | -29.345 | -3.705 | -84.5 | -195.695 |
| **700** | -75.11 | -142.7 | -166 | -63.2 | -40.11 | -3.99 | -91 | -205.01 |
| **750** | -83.975 | -153.75 | -178.75 | -75.1 | -50.875 | -4.275 | -97.5 | -214.325 |
| **800** | -92.84 | -164.8 | -191.5 | -87 | -61.64 | -4.56 | -104 | -223.64 |
| **850** | -101.705 | -175.85 | -204.25 | -98.9 | -72.405 | -4.845 | -110.5 | -232.955 |
| **900** | -110.57 | -186.9 | -217 | -110.8 | -83.17 | -5.13 | -117 | -242.27 |
| **950** | -119.435 | -197.95 | -229.75 | -122.7 | -93.935 | -5.415 | -123.5 | -251.585 |
| **1000** | -128.3 | -209 | -242.5 | -134.6 | -104.7 | -5.7 | -130 | -260.9 |
| **1050** | -137.165 | -220.05 | -255.25 | -146.5 | -115.465 | -5.985 | -136.5 | -270.215 |
| **1100** | -146.03 | -231.1 | -268 | -158.4 | -126.23 | -6.27 | -143 | -279.53 |
| **1150** | -154.895 | -242.15 | -280.75 | -170.3 | -136.995 | -6.555 | -149.5 | -288.845 |
| **1200** | -163.76 | -253.2 | -293.5 | -182.2 | -147.76 | -6.84 | -156 | -298.16 |
| **1250** | -172.625 | -264.25 | -306.25 | -194.1 | -158.525 | -7.125 | -162.5 | -307.475 |

These Free energies were then used to calculate the Gibbs' free energy of each decomposition reaction at the various temperatures using the above $\Delta G_r$ equation (with $\Delta G_f$ of products and reactant adjusted for stoichiometry). The calculated $\Delta G_r$ were then plotted for fructose as shown in Figure 2-4.

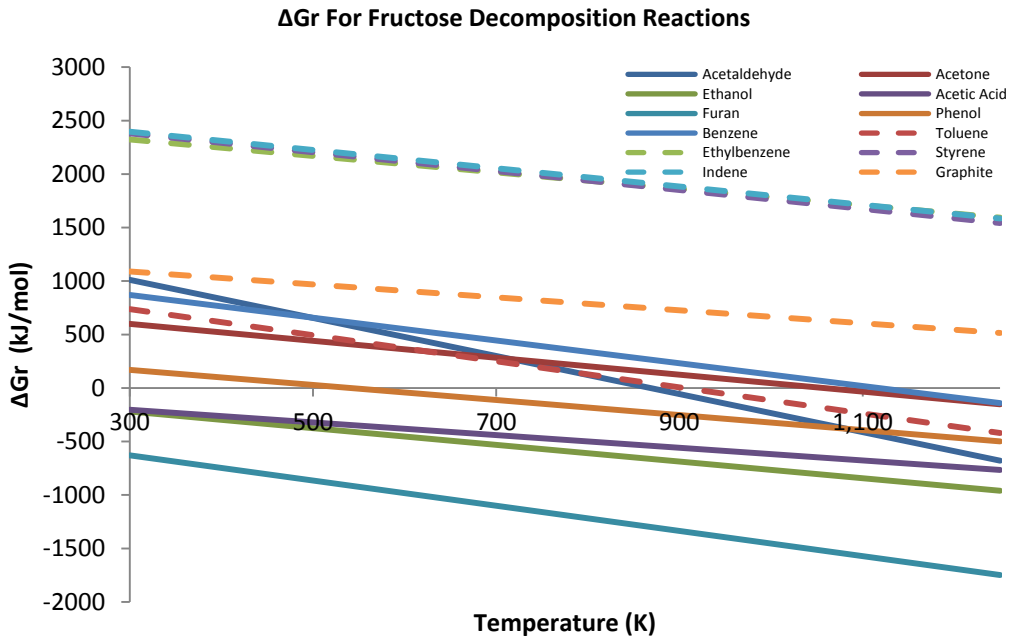


**Figure 2-4:** Gibbs' free energy of reaction for the twelve fructose decomposition reactions. Note that negative ΔGr does not necessarily require that reaction proceeds at room temperature. Analysis does not take kinetic limitations into account. Dashed lines are the reactions of interest that produce graphitic carbon and aromatics that can polymerize. Graphite reaction is ideal for producing CNTs.

The five reactions that produce graphitic carbon are shown by the dashed lines in the figure. Of those five reactions, only one is thermodynamically favorable at the temperatures being used for CNT synthesis, which explains the low carbon yield that was produced when fructose is pyrolyzed. Based on this analysis, there are two primary factors that negatively affect the carbon yield of this process. The first is the highly negative $\Delta G_f$ of fructose (<-1300kJ/mol) at room temperature prevents most of the carbon producing reactions from being favorable within the required temperature range. The second is the numerous oxygen atoms present in the fructose molecule. This high oxygen/carbon ratio means that more of the carbon will be released in the form of volatile organics and carbon dioxide, rather than being left behind as graphitic carbon residue. This fits well with experimental observation of negligible residual mass after annealing.

Using this information, we were able to add two new criteria to the precursor selection process. The ideal precursor must have a $\Delta G_f$ that is significantly less negative than fructose, allowing it to more readily decompose within the necessary temperature range. It also most have a high carbon/oxygen ratio in order to minimize the amount of carbon lost to organics and $CO_2$.

#### 2.3.2.2 1-Pyrenebutyric Acid

Based on our newly added criteria, 1-pyrenebutyric acid (PyBA) appears to be a much more viable candidate as a carbon precursor than fructose. The alkyloic acid group attached the the pyrene means that it will still be hydrophilic and thus, can still be adsorbed into the pores of the zeolite. Add to that the fact that PyBA has an approximate $\Delta G_f$ that is significantly less negative (~-275 kJ/mol) at room temperature than fructose and has a much higher ratio of carbon atoms to oxygen atoms in the structure (20:2).

Again, the $\Delta G_r$ for the formation of each compound was plotted against temperature from 300-1250 K. The results of which are shown in Figure 2-5.

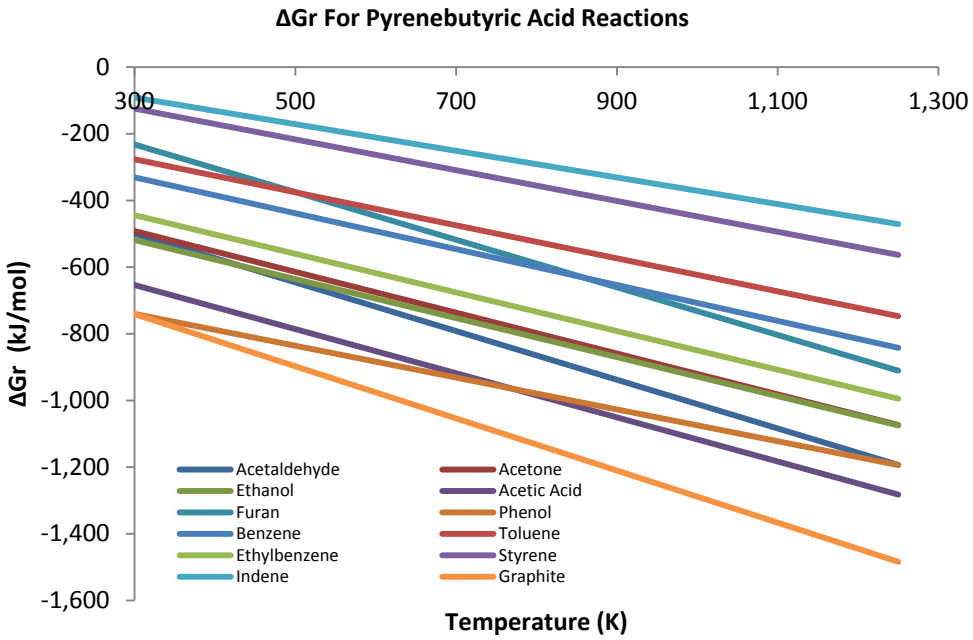


**Figure 2-5:** Gibbs' free energy of reaction for the twelve PyBA decomposition reactions. Note that negative ΔGr does not necessarily require that reaction proceeds at room temperature. Analysis does not take kinetic limitations into account. Due to high carbon content of PyBA, all reactions form graphitic carbon in some quantity and all reactions are thermodynamically favorable due to the low –ΔHf of PyBA.

It is immediately noticeable that all reactions are thermodynamically (albeit not necessarily kinetically) favorable over the entirety of the required temperature range. Add to that the fact that all of the reactions involved produce graphitic carbon and one would expect a significantly higher amount of graphitic carbon residue in the product and thus, would work better as a carbon precursor than fructose.

### 2.3.3 Thermogravimetric Analysis (TGA)

Thermogravimetric analysis (TGA) was used to determine the best method of absorption for the carbon precursors by determining how much graphitic carbon could be produced from each

absorption method. Each method showed three consistent stages, regardless of the absorption method, catalyst, and carbon precursor employed.

The first stage was the small weight loss around 100°C. This loss was due to the evaporation of residual water that was adsorbed into the VPI-5 pores. This result showed that it was necessary to add the water-purge stage to the beginning of the pyrolysis procedure.

The second distinct stage of the TGA experiment was the stage that involved the largest mass drop of the overall procedure and occurred between 250-600°C. This distinct region of the plot was due to the formation (and subsequent evaporation) of the various volatile organic compounds formed from the pyrolysis of the carbon precursor (As detailed in the thermodynamic analysis section).

The final stage of the experiment involved minimal weight loss after all of the volatile organics evaporated, from 600-1000°C, followed by a sudden weight loss at 1000°C after the introduction of air into the system. This section of the plot is the most important, as it determines (A) The lower limit of pyrolysis temperature, (B) The total percentage of carbon precursor that was adsorbed into the sample, and (C) The weight percent of graphitic carbon that could be extracted from the conditions tested.

### 2.3.4 Carbon Precursor Adsorption

PyBA was infiltrated into the VPI-5 using vacuum sublimation infiltration, using an AAO membrane as a barrier between unevaporated PyBA and VPI-5. Thermogravimetric analysis (TGA) was used to quantify graphitic carbon that could be created using this precursor and method of infiltration. The specimen was raised to pyrolysis temperatures under an inert N2 atmosphere at 10C/min. When pyrolysis temperature was reached, air was allowed into the system to burn away remaining carbon. The drop in mass percent was used to quantify the

percentage of amorphous carbon that was adsorbed in the zeolite. The mass drop was found to be about 3% before the cobalt was added and about 1% after the cobalt was added. Though, the cobalt drop is misleading, as it was affected by the mass increase due to the oxidation of the cobalt nanoparticles.

### 2.3.5 Determination of Optimal Pyrolysis Temperature

Since VPI-5 is not stable at high temperatures[5], it was necessary to determine the highest temperature at which the pyrolysis process could be carried out. To do this, the zeolite was annealed in an inert, argon atmosphere to various temperatures between 600-1000°C, with a hold at 100°C to purge any water prior to ramping to annealing temperature. X-ray diffraction patterns were then taken for each sample to determine if they retained the characteristic (100) diffraction peak, showing that they still had the 1.2nm pore that is required for synthesis of 0.8nm carbon nanotubes.

The XRD data collected shows that the (100) diffraction peak is completely removed when the temperature of the zeolite is raised above 700°C, even when all water is purged from the pores and no carbon precursor is adsorbed into the sample.

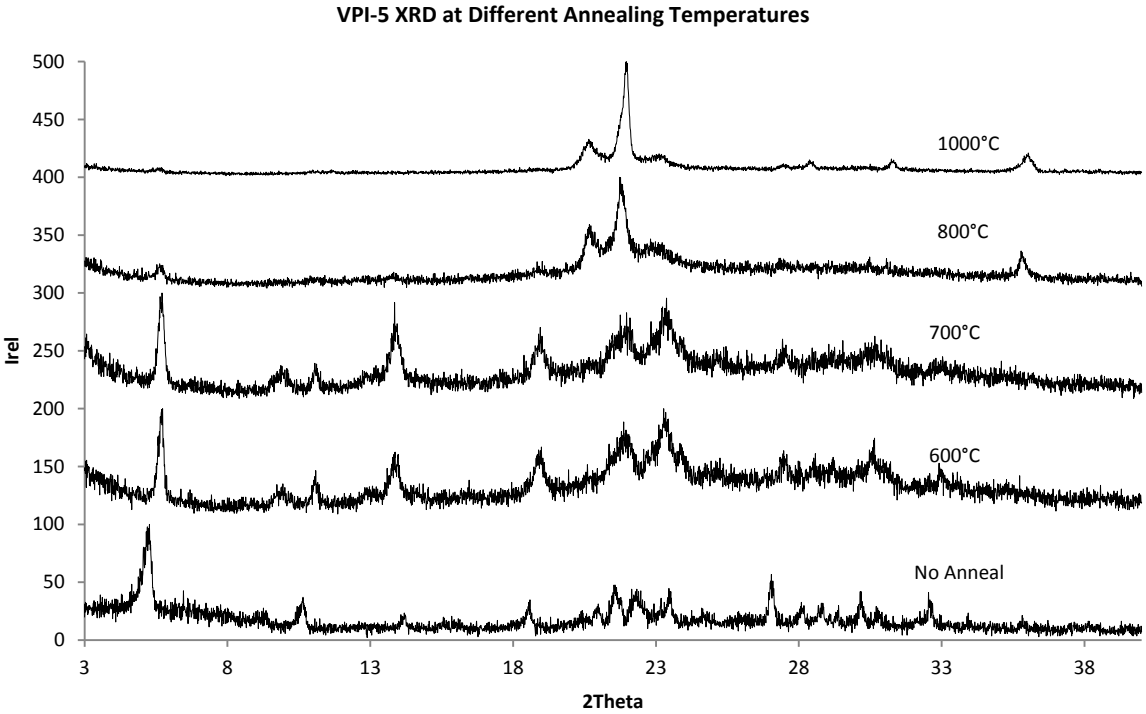


**Figure 2-6:** X-ray powder diffraction patterns of VPI-5 annealed at various temperatures. Experiment shows that VPI-5 pore structure does not remain stable above 700°C.

### 2.3.6 TGA Determination of Optimum Absorption Procedure

As a basis for comparison, the zeolite was analyzed on its own using TGA. Using this analysis, it was determined that a small amount of water was always trapped within the pores of the zeolite, thus necessitating that each high-temperature step of the synthesis procedure be accompanied by a hold at 100°C to purge out any water from the zeolite.

1-pyrenebutyric acid (PyBA) was then analyzed on its own to determine the amount of carbon residue it could produce. The sample showed the behavior that was predicted in the thermodynamic study, with a large mass reduction between 300-400°C due to PyBA decomposing into volatile organics, followed by a sharp drop in mass after air was introduced to the system. The overall mass drop was around 68%, with only about 3% due to graphitic carbon.

The PyBA was then tested with cobalt nanoparticles to examine its viability on its own as a carbon source for the nanoparticle catalyzed reaction. The sample showed the same behavior as the PyBA on its own, with the majority of the mass lost to volatile organics. The overall mass reduction was around 60%, with about 10% of that being from graphitic carbon, showing that the cobalt nanoparticle improved the amount of precursor that was converted to graphitic carbon.

VPI-5 was then infiltrated with PyBA via sublimation infiltration without the use of an AAO membrane barrier to determine the viability of that absorption procedure. The sample showed the same drop from water loss at 100°C, followed by the mass drop due to the decomposition of the PyBA and subsequent release of volatile organic compounds. The sample then showed about a 3% drop due to the carbon residue being burned away when air was introduced to the system. The overall drop in mass was around 35%. This high level of mass drop shows that the PyBA is not only adsorbed into the pores of the VPI-5, but also outside of the sample and physisorbed to the outer surface.

Finally, the VPI-5 was infiltrated with PyBA via sublimation infiltration with an AAO membrane barrier between the PyBA and the zeolite crystals. This extra step was implemented to prevent excess PyBA from being involved in the TGA analysis, as the previous analysis of the mechanically mixed sample showed a weight percent to be far too high to be due only to absorption in the pores. These samples were then analyzed using TGA to determine carbon content as well as total mass content. The results showed an overall mass drop of 18%, which is consistent with calculated estimates of the pore volume of the VPI-5. The analysis also showed that the graphitic carbon residue was around 3% (i.e. minimal difference between the two processes in terms of carbon content).

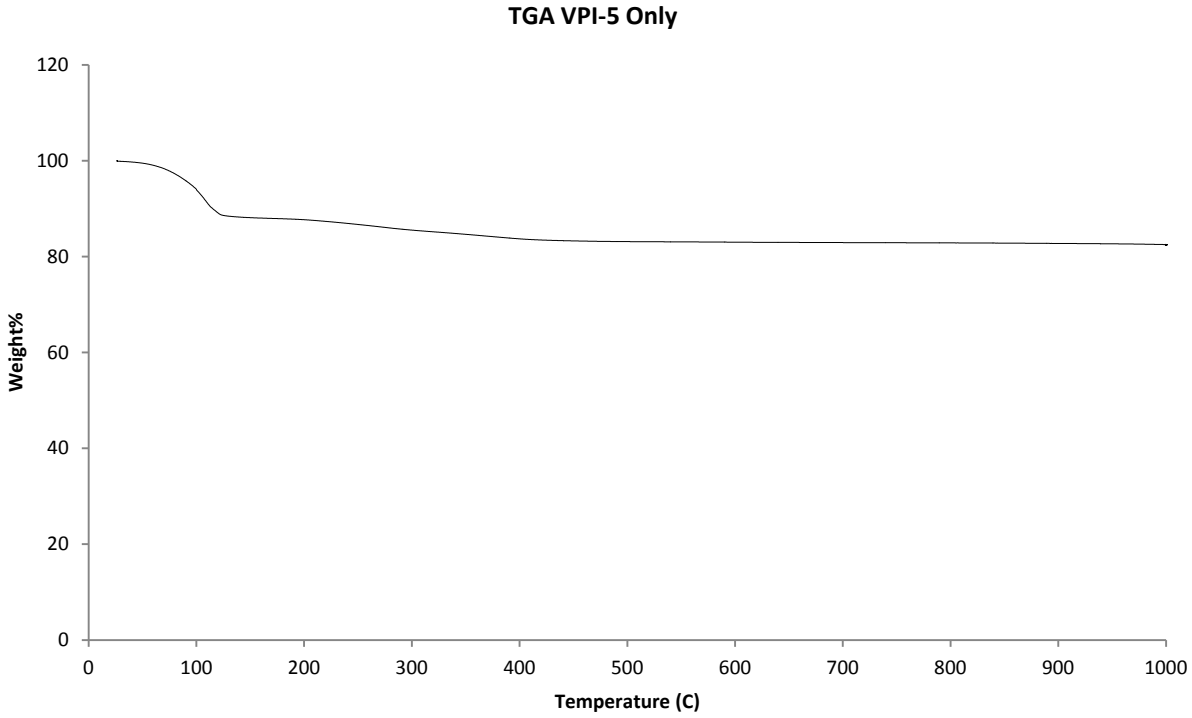


**Figure 2-7:** Thermogravimetric analysis of VPI-5 zeolite prior to absorption of 1-Pyrenebutyric acid.

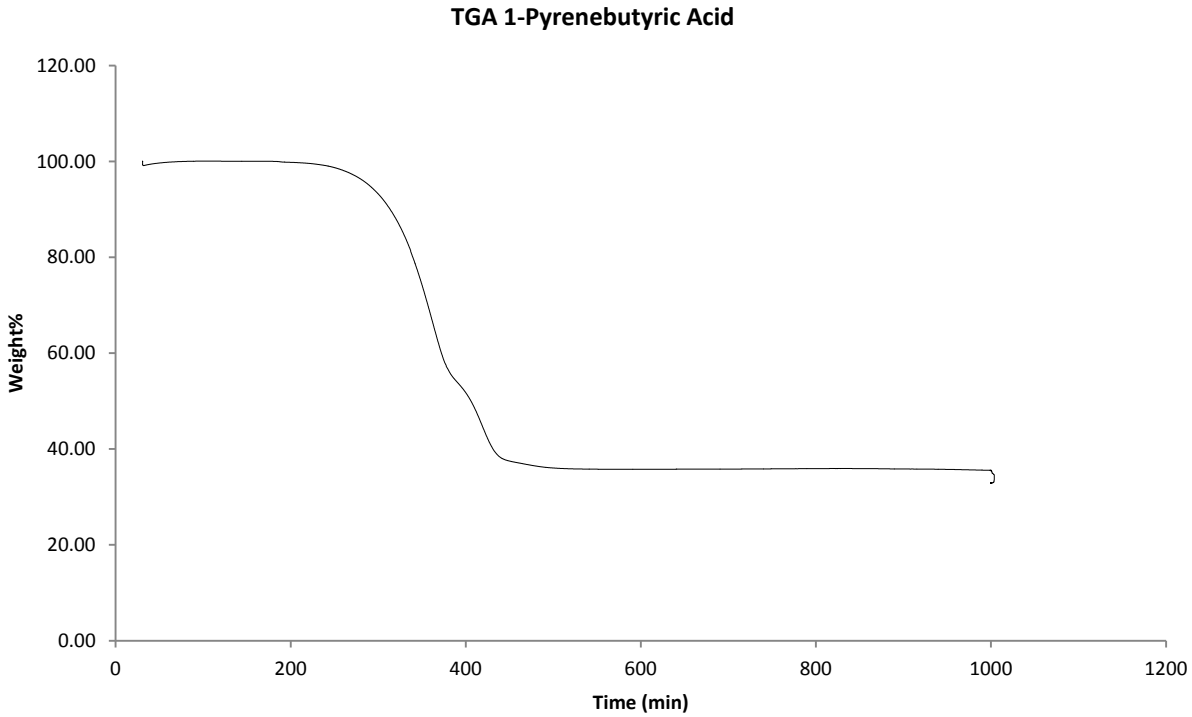


**Figure 2-8:** Thermogravimetric analysis of 1-pyrenebutyric acid without cobalt nanoparticle catalyst.

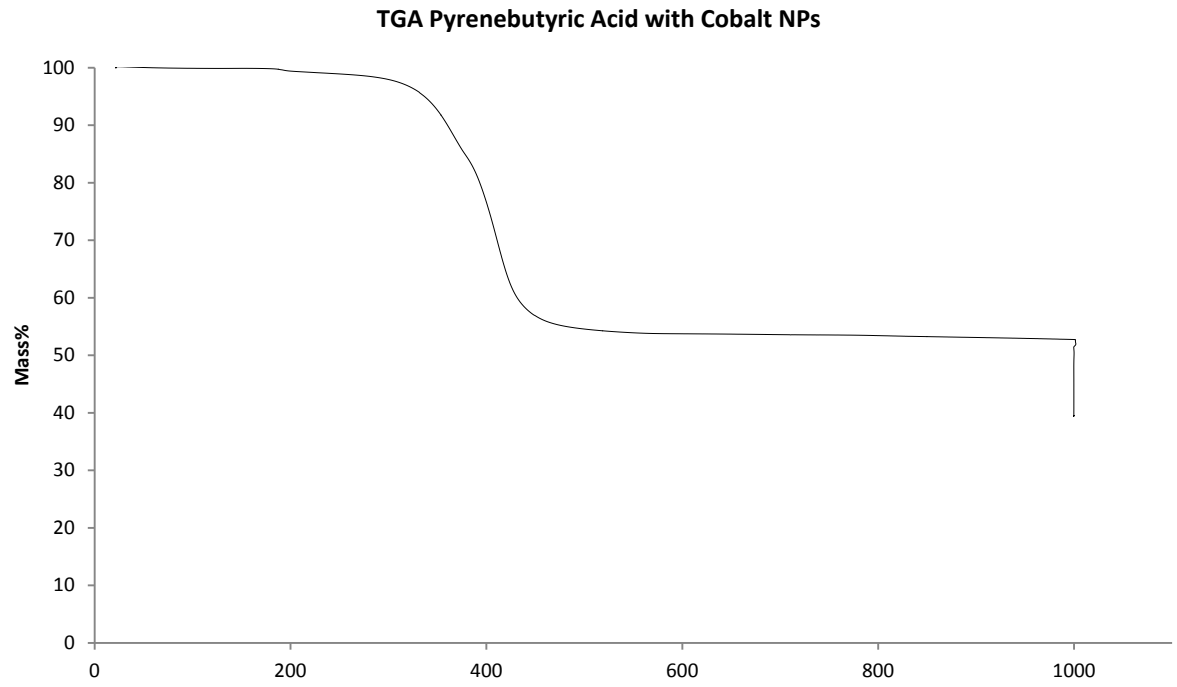


**Figure 2-9:** Thermogravimetric analysis of 1-pyrenebutyric acid with cobalt nanoparticles.

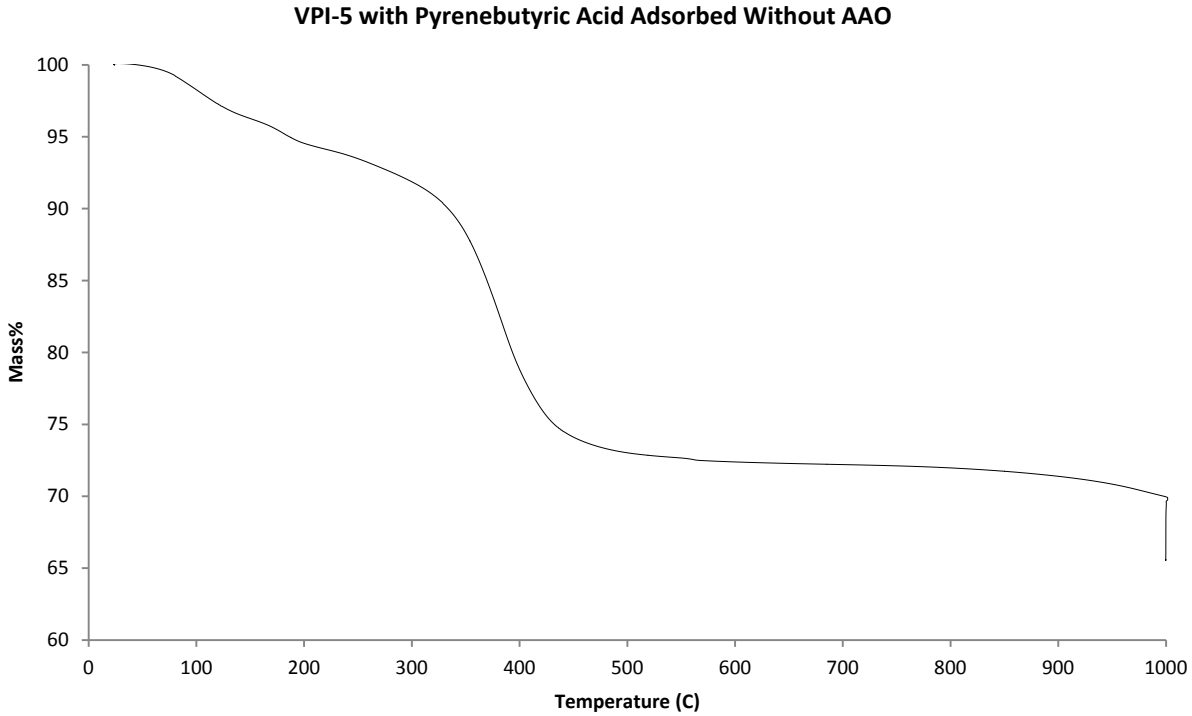


**Figure 2-10:** Thermogravimetric analysis of 1-pyrenebutyric acid with cobalt nanoparticle catalyst. Results show great improvement in graphitic carbon content by adding the catalyst.

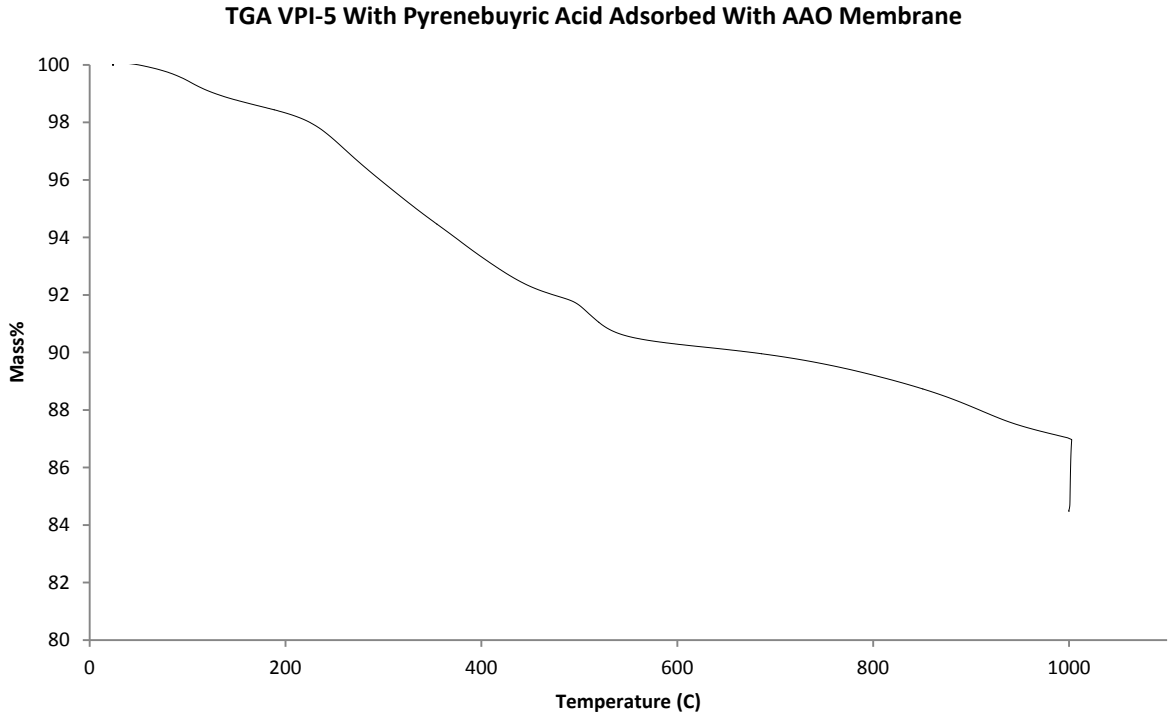


**Figure 2-11:** Thermogravimetric analysis of 1-pyrenebutyric acid adsorbed within the pores of VPI-5 zeolite with an AAO membrane barrier used during sublimation absorption.

### 2.3.7 Raman Spectroscopy of Pyrolysis Product

Raman spectroscopy is the most widely used characterization method for identification of carbon nanotubes[8,11]. Several characteristic bands can be used to identify the presence of single-walled carbon nanotubes, such as the vibration of the hexagonal structure of graphitic carbon (G-band) and the vibration that is induced by defects in the graphitic structure (D-band). The most informative band however, is the radial breathing mode (RBM) of the Raman spectrum. As the name suggests, this band is due to the wall of the CNT vibrating radially outward and inward ("breathing"). This band can be used, not only to distinguish the Raman spectrum of CNTs from graphitic carbon, but also to measure their approximate diameter. The

ideal CNT sample will contain a large ratio between the heights of the G-band to the D-band and will also show a well-defined, narrow RBM peak at $\omega=397cm^{-1}$.

The various synthesis parameters were evaluated on their ability to produce carbon nanotubes based on the Raman spectra obtained from the final product. The results are summarized in Table 2-6.

**Table 2-6:** Summary of Raman results for various experimental parameters, such as element and oxidation state of the transition metal catalyst, method of carbon precursor absorption, and post-pyrolysis treatments.

| Sample | Catalyst | Reduced | Catalyst In/Out | Abs with AAO | $H_2O_2$ Oxidation | Surfactant | G/D | RBM |
|---|---|---|---|---|---|---|---|---|
| **1** | Co | x | In | x | | | 0.98 | None |
| **2** | Co | x | Out | x | | | 0.97 | None |
| **3** | Co | x | In | x | x | | 0.97 | Weak |
| **4** | Co | x | Out | x | x | | 1.05 | None |
| **5** | Co | x | In | x | x | x | None | None |
| **6** | Co | x | Out | x | x | x | 1 | None |
| **7** | Co | x | In | | x | | 1.16 | None |
| **8** | Co | x | In | | | | 1.19 | None |
| **9** | Fe | x | In | x | x | | | None |
| **10** | Fe | x | In | x | | | None | None |
| **11** | Fe | | In | x | x | | | None |
| **12** | Fe | | In | x | | | | None |
| **Best** | Co | x | In | | | | 1.42 | Strong/Broad |

### 2.3.8 Best CNT Synthesis Procedure

Based on the Raman spectroscopic results obtained from altering the various synthesis parameters, the samples that most likely contain carbon nanotubes were synthesized using the following procedure.

VPI-5 zeolite was synthesized by the optimized procedure as described by Anderson, et al[5]. Zeolite crystals were then dried in a vacuum oven to remove any water from the pores. Sample was then immersed in solution of $CoCl_2$ and allowed to soak for 3 hours to adsorb $Co^{2+}$ ions into the pore structure of VPI-5. After the Co@VPI-5 crystals were filtered by vacuum filtration and dried in a vacuum oven, they were immersed in a solution of sodium borohydride ($NaBH_4$)in water to reduce $Co^{2+}$ ions to Co nanoparticles. These crystals were then collected by vacuum filtration and dried in a vacuum oven overnight. Sample was then mechanically mixed with 1-pyrenebutyric acid (PyBA) and placed in an alumina boat before being transferred into the tube furnace. The tube furnace was then placed under vacuum using a vacuum pump. The sample was then heated to 100°C at a rate of 2°C/min and maintained at that temperature and pressure for 1 hour, before raising the temperature to 150°C at a rate of 2°C/min and holding for 4 hours. After they were cooled to room temperature, the VPI-5 crystals were removed from the furnace and excess PyBA was washed from the surface with acetone. Co@VPI-5 with PyBA inside pores was then placed back in the alumina boat in the furnace and was purged 5 times using argon gas. The temperature was raised to 650°C under flowing argon (again, with a 100°C water purge step) and held at this temperature for 1 hour. After it was cooled back to room temperature, the product was recovered and placed in 10% HCl to dissolve away the zeolite template.

Raman spectrum of this sample showed the largest G/D ratio among all synthesis attempts along with the most well-defined RBM peak, showing strong promise to the presence of 0.8nm single-walled carbon nanotubes.

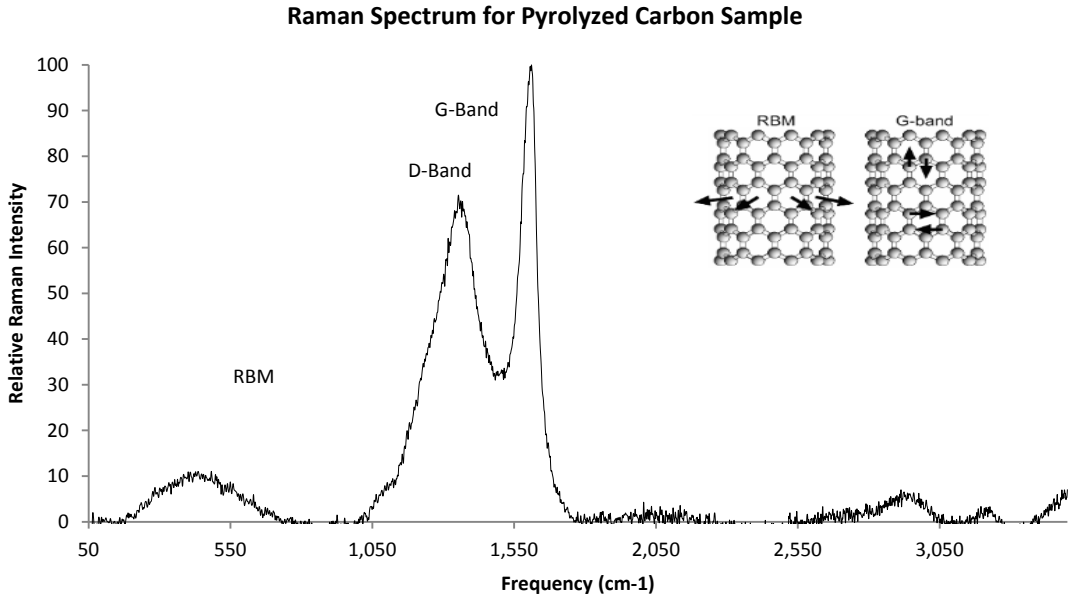


**Figure 2-12:** Raman spectrum of pyrolyzed carbon sample, showing graphite-related (G-band), defect-induced (D-band), and Radial Breathing Mode (RBM). Inset: diagram of RBM and G-band.

## 2.4 Conclusions

In summary, VPI-5 zeolite has been synthesized in order to fabricate single walled carbon nanotubes of diameter 0.8nm for water desalination applications. Raman spectroscopy shows promising results for the presence of carbon nanotubes, but the presence of amorphous carbon in the final product made it difficult to determine if CNTs were present. Additionally, the broad RBM peak made it impossible to get any more than an approximation of the diameter of the synthesized nanotubes.

X-ray diffraction studies were used to determine the optimum pyrolysis temperature by annealing the VPI-5 to various temperatures. It was found that the zeolite structure decomposed at temperatures above 700°C, making CNT synthesis above those temperatures impossible.

A study of the thermodynamics of the pyrolysis process revealed 1-pyrenebutyric acid (PyBA) to be a more than suitable carbon precursor. Previous studies of this process have shown that sugar compounds such as fructose and sucrose can produce carbon nanotubes in low yields, but they also produce water during pyrolysis, causing decomposition of the zeolite structure. Using PyBA as the carbon precursor should minimize the production of water and thus maximize the ability to produce CNTs in large quantities.

# Ch. 3: Monolayer Plating of Precious Metals on Insulating Mesoporous Supports

## 3.1 Introduction

The need for clean, renewable energy is one of the most important problems that face the world today. Hydrogen energy has emerged as one of the leading candidates to replace the current fossil fuel based energy industry. One of the most attractive processes for the generation of hydrogen power is proton exchange membrane (PEM) water electrolysis. These types of devices have several features that make them viable candidates for these applications, such as low temperature of operation, high current density, low weight, and compact design[67]. The primary hurdle faced by these industries is the prohibitively high cost of the devices. The most expensive part of these devices is the precious metal catalyst. Generally, platinum is used as the cathode of the device for the hydrogen evolution reaction (HER) and iridium is used at the anode for the oxygen evolution reaction (OER). These metals are required for two main reasons. The first is they yield the best catalytic activity for the two necessary reactions in acidic systems. The other is that, due to the strong acidity of the electrolyte, a highly noble metal is required to prevent corrosion of the catalyst[22].

Platinum (among other precious metals) is also commonly used in for numerous catalytic applications, including the electrooxidation of methanol in direct methanol fuel cells[70]. It is also used as a hydrogenation catalyst for unsaturated hydrocarbons[71] and used for the decomposition of hydrogen peroxide[72]. The most common use of platinum catalysts, however, is for the oxidation of carbon monoxide (CO) and complete combustion of exhaust hydrocarbons ($C_xH_y$) in automobile catalytic converters. In all of these devices, there is room for cost reduction by improving the efficiency of the catalyst.

Extensive research has gone into maximizing the efficiency of the catalyst and therefore minimize the cost of the device. Currently, the state of the art practice is to use nanoparticles (~2 nm) of the precious metal on mesoporous supports, such as high surface area carbon[19,22,38] or zeolite[32] materials. This practice still only leaves about 30% of the atoms on the surface and thus available for catalysis. The ideal situation would be to use a monolayer of catalyst on a highly porous support material, making all atoms in the device available for catalysis and allowing the substance to make maximum contact with the catalyst material.

The underpotential deposition of Cu has previously been demonstrated to plate a monolayer of platinum by first depositing a monolayer of Cu atoms at a different voltage than bulk. This process occurs when the copper atoms are more strongly bound to a foreign substrate than to atoms of their own kind, which results in the deposition of anywhere between one and three monolayers[26]. The Cu monolayer can then be monotonically replaced by platinum (or iridium) atoms due to their difference in reduction potential[35].

This method for monolayer plating has been extensively studied, but has thus far only been demonstrated using conductive substrates. Most notably, this process has been demonstrated on gold substrates, such as Au(III)[24] and nanoporous gold (NP Au)[25]. It has also been used to plate a monolayer onto carbon nanotube mattes[20], or create core-shell nanoparticles, where some conductive nanoparticle substrate, such as Au or Pd is plated with a platinum monolayer shell[14,66] . Gold, or other precious metal substrates, however, are not suitable for the purposes of cost reduction due to their similar costs to that of platinum.

In this work, we demonstrate the ability to use the underpotential deposition and redox replacement method to plate a platinum or iridium monolayer onto an insulating mesoporous support by first depositing a conductive layer on one face of the support. By showing that a

platinum monolayer can be plated from the conductive face across the pores of the membrane, we show that the copper plates via a novel growth front mechanism, where initial nucleation of the monolayer happens on the conductive face, followed by monolayer growth on the insulating surface of the substrate as shown in Figure 3-1.

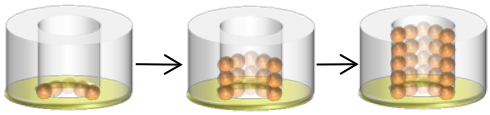

**Figure 3-1:** Proposed copper monolayer growth front mechanism. Copper monolayer nucleates at the conductive face of the membrane and grows through the pores of the membrane.

## 3.2 Experimental

### 3.2.1 Materials and Equipment

Anopore inorganic membranes (Anodisc) with support ring, 25 mm diameter, 0.02 µm pore size were obtained from Whatman.

Reagent grade $K_2PtCl_4$ and $IrCl_3 \cdot xH_2O$ were both obtained from Sigma-Aldrich.

X-ray photoelectron spectroscopy (XPS) was carried out using a Thermo Scientific K-Alpha X-ray photoelectron spectrometer.

Inductively coupled plasma optical emission spectroscopy (ICP-OES) was carried out using a Varian Vista Pro ICP-OES.

Electrochemical measurements were done using an eDAQ quadstat four channel potentiostat, using Ag/AgCl reference electrode and a platinum counter electrode.

## 3.2.2 Monolayer Plating

A general diagram of the monolayer plating process is shown in Figure 3-2.

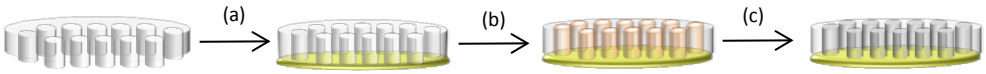


**Figure 3-2:** General overview of monolayer plating process, including (a) Deposition of gold film onto one face of an AAO membrane, (b) Cu monolayer UPD at 0.240V, and (c) Redox replacement of Cu with Pt to form Pt monolayer.

Using thermal evaporation, a 5 nm thick layer of Au was coated on one face of anodic aluminum oxide (AAO) membranes (Whatman).

The membranes were then soaked in 10 mL of 5 mM $CuSO_4 \cdot 5H_2O$ for 2 hours to allow $Cu^{2+}$ cations to fill pores of the membrane.

The membrane was then set up in a three electrode cell, acting as the working electrode with a platinum wire counter electrode and Ag/AgCl as the reference electrode.

The electrolyte solution consisted of 100 mL of 5 mM $CuSO_4 \cdot 5H_2O$ and 0.1 M $H_2SO_4$ and was deareated by bubbling with Ar gas for 30 min prior to the deposition in order to remove any $O_2$ from the solution and the sample surface.

Underpotential deposition was carried out by applying 0.240 V (vs. Ag/AgCl) to the sample in the potentiostat setup for 8 minutes. Following the Cu deposition, the membrane was immediately placed in a 1 mM solution of $K_2Cl_4Pt$ (Sigma-Aldrich) (or $IrCl_3 \cdot xH_2O$ for iridium plating) and held there for 10 min to monotonically replace Cu atoms with precious metal. The membrane was then moved to 10 mL deionized water and left there for 10 min to remove any $Pt^{2+}$ or $Ir^{3+}$ cations that could have physisorbed to the surface.

### 3.2.3 Characterization

X-ray photoelectron spectroscopy was used to determine presence of the platinum (or iridium) on the membrane surface that was not coated with gold.

Inductively coupled plasma optical emission spectroscopy (ICP-OES) was used to quantify the platinum (or iridium) that was plated on the surface of the membrane. After monolayer plating was completed, the membrane was placed in 10% $HNO_3$ and heated to 100°C for 3 hours to digest sample and get analyte atoms into solution. Calibration curve was constructed using 5, 1, 0.5, 0.1, and 0.05 ppm standard solutions of the analyte.

The catalytic activity of the monolayer plated membranes was then tested with electrochemical water electrolysis via cyclic voltammetry.

Control membranes were coated with a 5 nm thick layer of gold and then soaked in $K_2PtCl_4$ ($IrCl_3 \cdot xH_2O$) solution for 10 minutes, followed by a 10 minute rinse in DI water.

## 3.3 Results/Discussion

Membranes were tested for monolayer coverage using ICP-OES spectroscopy and x-ray photoelectron spectroscopy (XPS) and for catalytic activity using electrochemical water electrolysis. ICP-OES was used to quantify the precious metal in the samples in order to determine that a monolayer was forming on the entire surface area of the membrane, rather than simply on the face that was plated with gold. XPS was used to prove that the metal was plated on the non-conductive surface. Since the only way platinum could be plated on the non-conductive surface by nucleating on the conductive face and growing through the pores, this result will show evidence of a growth front mechanism.

### 3.3.1 Platinum Monolayer

Platinum plated membranes were dissolved in 10 mL of 10% nitric acid and analyzed using inductively coupled plasma optical emission spectrometry (ICP-OES) to determine if platinum monolayer was forming in pores of membrane or simply on conductive face of membrane. The surface area of the membrane was estimated using the porosity (0.25) and thickness (30 μm) of the membrane provided by Whatman, and assuming that the pores were cylindrical and 20 nm in diameter through half of the membrane and 200 nm in diameter for the other half of the membrane, based on the fact that the pores branch off of one another and change diameter throughout the membrane. Using this surface area, the concentration of platinum that can be expected in a 10 mL diegested sample could be calculated. The results are summarized in Table 3-1.

**Table3-1:** Predictions of ICP data for Pt monolayer deposition on Au surface only vs full membrane surface. Measured value of **5.53±0.4 μM** suggests that monolayer is plated on full membrane

| | **Monolayer on Au Surface** | **Monolayer on Full Membrane Surface** | **Measured Value** |
|---|---|---|---|
| Calculated Surface Area ($m^2$) | 0.000137 | 0.00524 | -- |
| Calculated Concentration of Pt (μM) | 0..403 | **5.59** | **5.53±0.4** |

ICP-OES analysis shows that the dissolved AAO membrane contained an average concentration of 5.53±0.4 μM of platinum. Based on the calculated estimate, the sample would only be 0.403 μM if the monolayer was only plated on the conductive face of the membrane. The calculated estimates predict that coating the entire surface of the membrane, including the conductive face, the pores, and the insulating face would result in a 5.59 μM sample solution. Since the

actual concentration of the digested sample adhered more closely to the estimates of full membrane coverage, this test is the first step in proving the monolayer coverage via copper growth front mechanism.

Since quantifying the amount of platinum plated on the sample still leaves the possibility of bulk plating on the conductive surface, plated membrane was also analyzed with XPS to determine if platinum was plated on the insulating surface. Platinum 4d peaks between binding energies of 350 and 315 eV were used to determine platinum presence due to primary peak overlap with Al 2p binding energy. The results of the analysis are shown in Figure 3-4.

XPS analysis shows faint platinum 4d doublet peaks, proving that small amounts of platinum are present on the insulating face of the membrane. These small amounts are to be expected due to the fact that secondary peaks had to be analyzed for this experiment as well as the small amount of platinum that would be associated with a monolayer. This goes on to further demonstrate the copper monolayer growth front mechanism, since the copper would not be able to plate on the insulating face of the membrane without first nucleating on the conductive face and growing across the pores of the membrane.

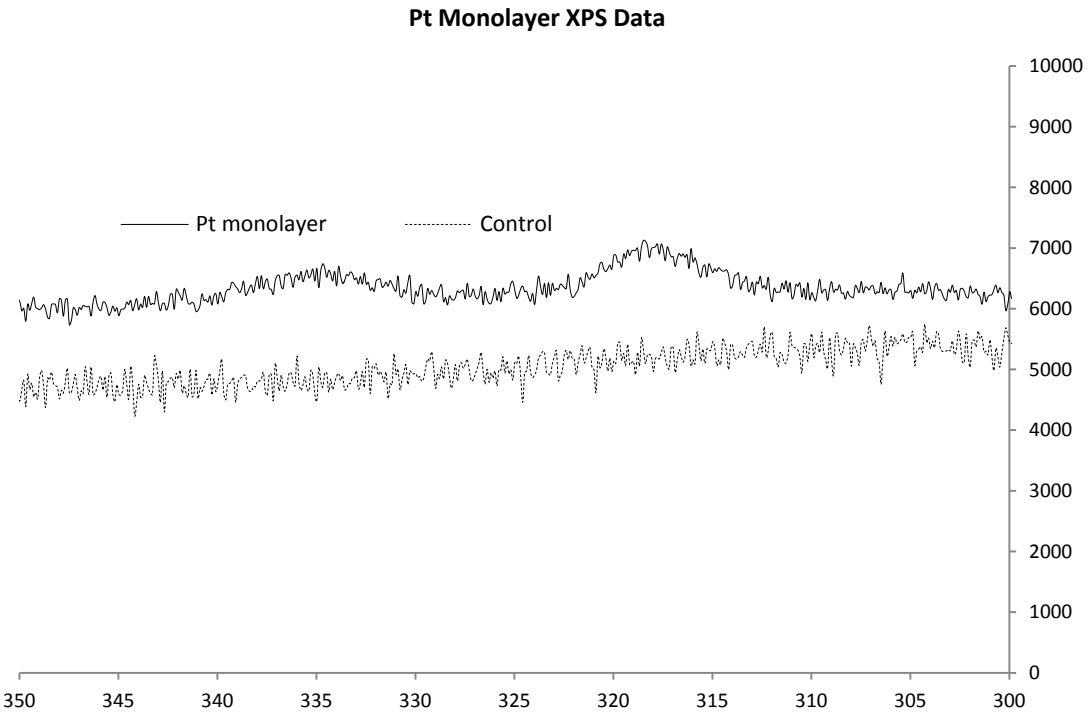


**Figure 3-3:** XPS analysis for 350-315 eV region shows small amounts of Pt are plating on surface opposite Au face. Control membrane was Au sputtered, soaked in $Pt^{2+}$ and rinsed in DI water

After demonstrating that a monolayer of platinum could be plated onto an insulating support, the catalytic activity of the membranes was tested using electrochemical water electrolysis via cyclic voltammetry. Samples were subjected to 10 cycles between -0.35V and 1.0V (vs. Ag/AgCl) with the membrane as the working electrode and a platinum wire as the counter electrode in deaerated $H_2SO_4$. Control sample showed very low ionic current with the applied potential, without showing any reduction-oxidation behavior. Platinum monolayer membrane shows clear electrochemical activity, with an onset voltage for the water splitting at around 0.80V. Though it does show different behavior than the standard behavior that is associated with bulk platinum[33], redox peaks clearly show electrochemical activity, with a peak at 0.606 V, shifted cathodically from the reference due to the particle size effect, where cathodic shift occurs as a

result of smaller particle size as compared to a bulk sample[69]. The gradual decay in current is likely due to loss in platinum surface area from particle formation during electrolysis.

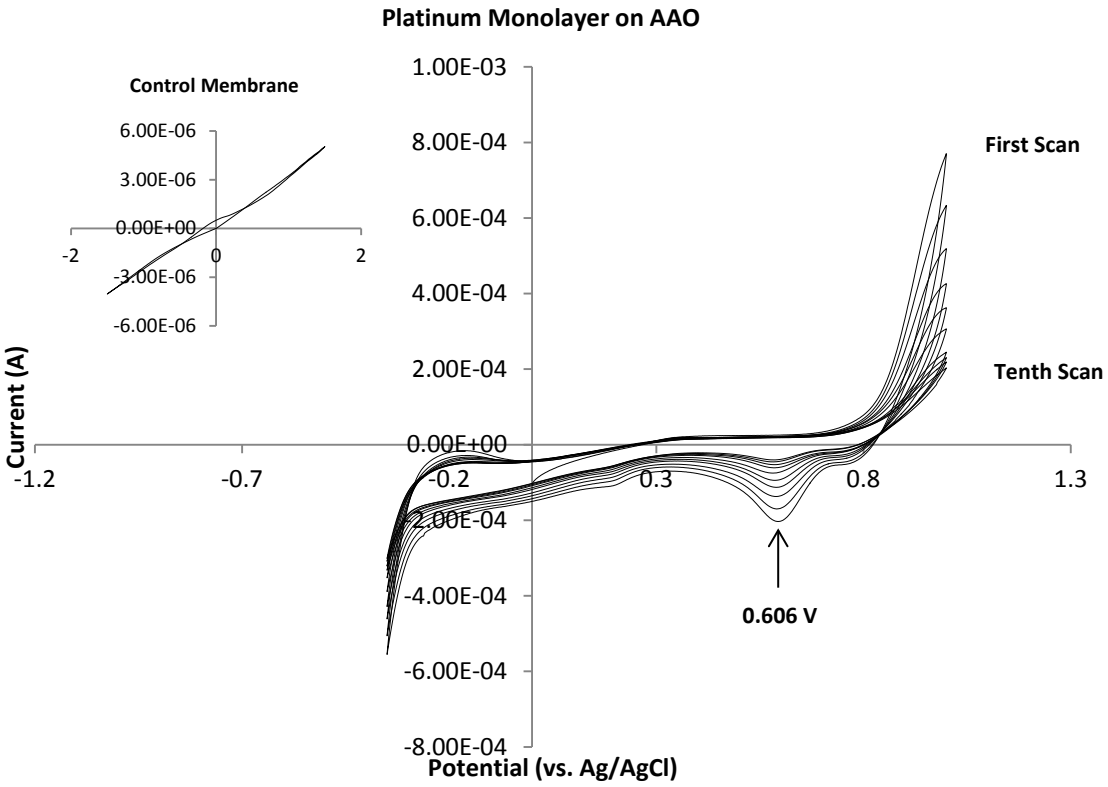


**Figure 3-4:** Cyclic voltammagram of AAO plated with platinum monolayer in deaerated, 0.1 M sulfuric acid with 0.1 M KCl. Plot shows ten scans. Inset: control membrane that was coated only in a thin film of gold.

## 3.3.2 Iridium Monolayer

The effects of a monolayer of iridium plated on AAO membranes were also studied, in order to show that this process can be used to improve both the hydrogen and oxygen evolution reactions in hydrogen production devices. These membranes were also characterized using XPS to determine presence of iridium on the surface opposite the gold coated face. Iridium 4f peaks

between 60-70 eV were used to determine iridium presence, as they do not overlap with aluminum 2p peaks, as was the case with platinum. As shown in Figure 4, iridium is clearly detected in the sample against the control. Since the XPS signal was stronger than expected, ICP-OES analysis was repeated for iridium monolayer membranes. The estimated surface area and the expected concentration of iridium sample was calculated in the same way as above. As was observed with platinum, ICP-OES shows that the quantity of iridium on the surface of the membrane (6.67±3.0 μM) was more consistent with a monolayer over the entire surface of the membrane (6.01 μM), rather than simply plating on the gold face (0.421 μM).

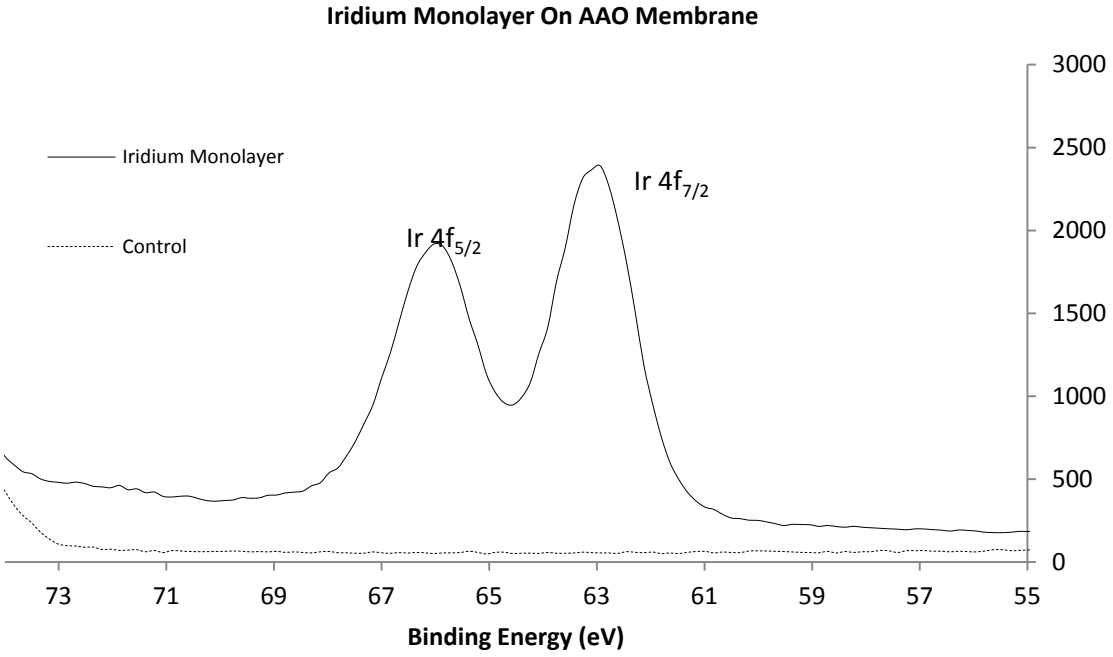


**Figure 3-5:** XPS spectrum for AAO membrane plated with iridium monolayer shows characteristic binding energies for Ir 4f orbitals.

**Table 3-2:** Predictions of ICP data for Ir monolayer deposition on Au surface only vs full membrane surface. Measured value of **6.67±3.0 μM** suggests that monolayer is plated on full membrane

| | **Monolayer on Au Surface** | **Monolayer on Full Membrane Surface** | **Measured Value** |
|---|---|---|---|
| Calculated Surface Area ($m^2$) | 0.000137 | 0.00524 | -- |
| Calculated Mass of Ir (μM) | 0.421 | 6.01 | 6.67±3.0 |

Since the iridium monolayer plated membranes showed similar results from ICP-OES and XPS characterization, the catalytic activity of these samples was then tested with the same electrochemical water electrolysis. Voltammetric curve for iridium in Figure 3-7 shows two main regions of electrochemical activity. The first, between 0-0.5V (vs. Ag/AgCl) is the hydrogen adsorption region, which is distinguished by a large oxidation peak, followed by the formation of a new oxide species, associated with the peak around 0.65 V. In this second area, the Ir was initially oxidized to an Ir(III) species. The shape of this voltammagram is consistent with reference[23].

Due to iridium oxidation, the sample tended toward loss of conductivity after only one potential cycle. In order to keep the sample conductive through more than one cycle, a monolayer of gold was plated onto the membrane before the iridium, using the same underpotential deposition and redox replacement method. The overall redox behavior of the iridium is still observed, although though the hydrogen adsorption peak still diminishes due to loss of surface area caused by IrO2 particle formation. Since gold has a low affinity for iridium oxide, this becomes

an issue of surface migration of the monolayer. This formation of particles also accounts for the shift in potential for the oxidation peak due to the particle size effect. This further indicates that the monolayer plates on the entire membrane, rather than the conductive face, as the gold monolayer would have no effect on the conductivity if it was only plating on top of a thick film of gold.

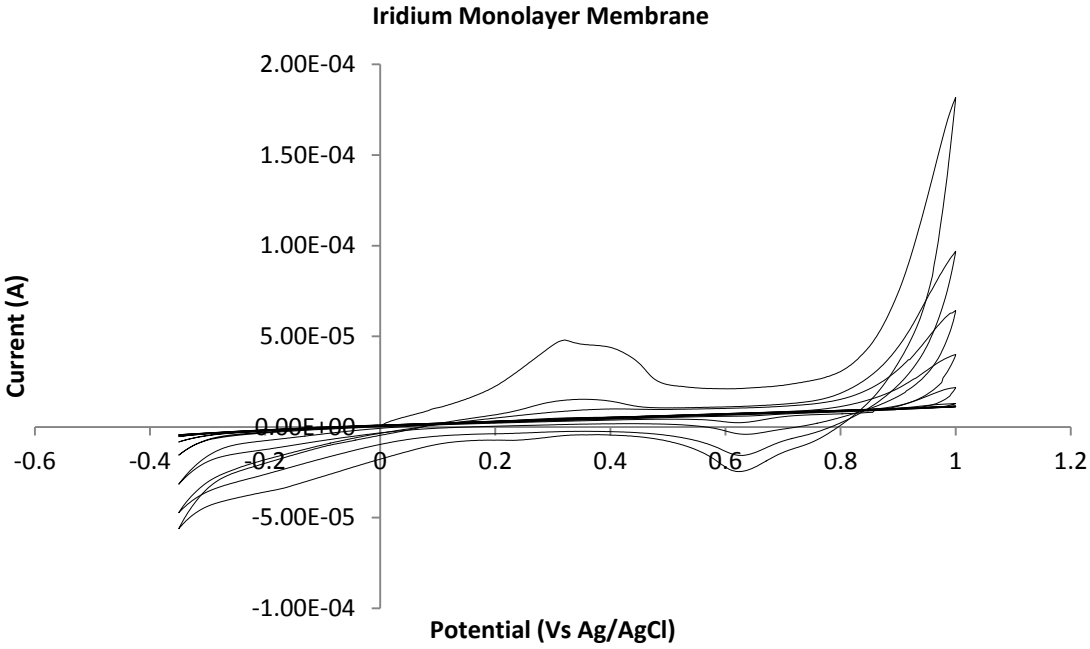


**Figure 3-6:** Cyclic voltammagram of AAO plated with iridium monolayer in deaerated, 5 mM sulfuric acid with 0.1 mM KCl. Sample loses conductivity rapidly and catalytic activity is reduced.

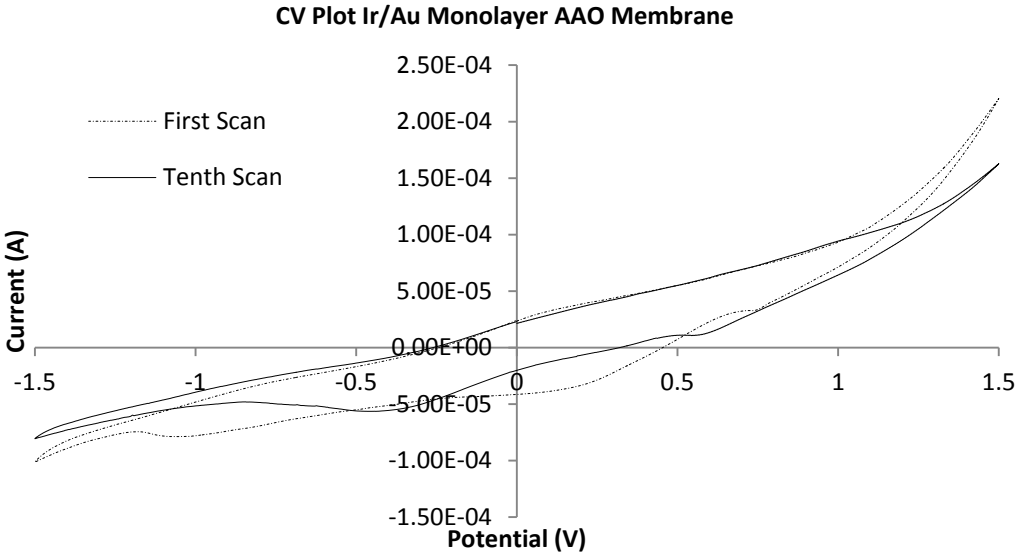


**Figure 3-7:** Cyclic voltammagram of AAO plated with gold/iridium monolayer in deaerated, 5 mM sulfuric acid with 0.1 mM KCl. Plot shows 10 scans and demonstrates gold monolayer improving conductivity of monolayer plated membrane.

## 3.4 Conclusions

We have for the first time succeeded to plate a precious metal monolayer onto an insulating support using the underpotential deposition of copper, followed by the redox replacement by precious metal. This demonstrates a novel copper monolayer *growth front* plating mechanism. While the plating of the precious metal was successful, one issue that faces the process is loss of catalytic activity after only a few potential cycles. We hypothesize that this issue can be attributed to surface migration of the catalyst atoms, resulting in particle formation and loss of surface area. Further study is needed to mitigate this issue.

Since membranes show efficient mass transport, this allows for efficient flow across the surface of the catalyst, while minimizing the quantity of catalyst used and maximizing its efficiency. Applications for these membranes include polymer electrolyte membrane fuel cells, hydrogen production through water splitting, flow battery energy storage, and electrocatalytic conversions. This process can be used to lower the cost of these devices, thereby making them a more viable alternative energy source in the future.

# Ch. 4 – Conclusions and Future Work

## 4.1 Conclusions

### 4.1.1 Zeolite Templated Carbon Nanotube Synthesis

Virginia Polytechnic Institute number 5 (VPI-5) zeolite was used in an attempt to synthesize single walled carbon nanotubes (CNTs) with a uniform diameter of 0.8 nm. These nanotubes were to be used to fabricate an ideal CNT membrane for water desalination. X-ray diffraction was used to confirm the synthesis of VPI-5. Raman spectroscopy of the final pyrolysis product showed encouraging results for the presence of CNTs, based on a reasonable G/D ratio and a strong RBM peak. The presence of amorphous carbon, however, made it difficult to confirm the presence of CNTs via TEM imaging. Also, the broad RBM peak made only an approximation of the CNT diameters possible.

X-ray diffraction was also used to study the effects of high temperature on the structural stability of the zeolite. It was found that the VPI-5 pore structure decomposed at temperatures higher than 700°C. This study was used to determine that CNT synthesis within the pores could not be done at any temperatures higher than this.

Additionally, a thermodynamic study of the pyrolysis process was conducted to determine a suitable carbon precursor for this synthesis. The results of this study showed that 1-pyrenebutyric acid (PyBA) was better suited to the pyrolysis reaction than fructose, which had been previously used to produce CNTs in low yields. PyBA proved to be a more suitable precursor due to its low oxygen and hydrogen content, as well as its ability to produce large amounts of graphitic carbon when pyrolyzed. Using PyBA as a carbon precursor should minimize the amount of water produced during the synthesis, and thus minimize the tendency of VPI-5 to decompose at high temperatures and maximize the ability to produce CNTs in large quantities.

### 4.1.2 Monolayer Plating of Precious Metals

For the first time, we have demonstrated the ability to plate a monolayer of platinum and iridium onto an insulating support material using the underpotential deposition of copper, followed by the redox replacement of the more noble metal. This process has the potential to greatly improve the efficiency and decrease the cost of many catalytic devices.

In doing so, we show evidence of a copper growth front plating mechanism, wherein copper monolayer first nucleates on a conductive surface and grows through the insulating pores of an aluminum oxide support. By taking advantage of this growth front, we can potentially plate a monolayer of precious metal onto other porous oxide materials, provided there is a conductive film on one surface of the material.

Since membranes show efficient mass transport, this allows for efficient flow across the surface of the catalyst, while minimizing the quantity of catalyst used and thus, maximizing its efficiency. Applications for these membranes include polymer electrolyte membrane fuel cells, where they can improve the production of hydrogen through water splitting. Flow battery energy storage, and electrocatalytic conversions are also areas where the ability to maximize catalyst efficiency is a major concern. This process can be used to lower the cost of these devices, thereby making them a more viable alternative energy source in the future.

## 4.2 Future Work

### 4.2.1 Zeolite Templated Carbon Nanotube Synthesis

The ability to synthesize single-walled carbon nanotubes of uniform diameter using VPI-5 zeolite as a template could provide new opportunities for an ideal water desalination system due to the high fluid flow that carbon nanotube membranes provide along with the ability to exclude salt ions. Results from this work show great promise toward the ability to synthesize 0.8 nm diameter CNTs, but further study of the impregnation and formation of the transition metal nanoparticle catalyst is still needed to make this synthesis a reality. These CNTs can then be embedded in an epoxy matrix and microtome sliced to fabricate 5 μm carbon nanotube membranes. With this membrane fabricated, further study must be conducted into the fluid flow, separation ability, and fouling resistance.

These desalination membranes are the first step toward the capability of fabricating a charge-driven molecular water pump. In this system, a combination of charges can be positioned along the nanopore. Previous work in molecular dynamics simulations have shown that by placing the charges at specific positions along the nanopore can cause improved water flux through the pores of the membrane at 1 atm of pressure. This process is made possible by taking advantage of the charge dipole-induced ordering of water that is confined in nanochannels.

The entrances and exits to the membrane can also be chemically modified in order to improve the selectivity. Much research has been conducted in the past in the functionalization of carbon nanotube membranes and the attachment of actuated “gatekeeper” molecules that can mimic the behavior of proteins can be used to select particular chemical species from a solution. This species can then be pumped through the CNT membrane, mimicking the fast fluid flow of

natural aquaporins. Upon flowing through the membrane, the species can then come into contact with catalyst material at the exit to the pore. Using this type of work, the overall goal of mimicking natural enzyme systems can come to fruition.

### 4.2.2 Monolayer Plating of Precious Metals

The ability to plate a monolayer of precious metals onto a highly porous, insulating support is a great step forward in the field of catalysis. Since the high cost of most catalytic devices can be attributed to the precious metal catalyst, it is imperative to maximize its efficiency in order to make it economically viable. One of the main issues with this process is the formation of particles of the precious metals after only a few voltammetric cycles. This problem is primarily due to the surface migration of the catalyst atoms along the surface of the support. We speculate that this is caused by the low affinity that the atoms have for the substrate. Further research is needed to find ways to modify the surface of the support to prevent this migration.

Similarly to water splitting, the electrooxidation of methanol or ethanol is commonly used for fuel cell energy storage. Further research into this catalyst's efficiency with this reaction is also a necessity for the advancement of energy production and storage.

Further research for this process will involve plating a monolayer onto other substrates, such as $TiO_2$ and be tested for photocatalytic water electrolysis. Much research has gone into the ability to split water using methods involving solar energy. The two major hurdles that solar energy faces are high cost and intermittent production of energy. The ability to lower the costs of these devices by using as little of the precious metal catalyst as possible should prove to be a great advancement in the technology. The other major hurdle to the industry is also addressed by the ability to improve the catalytic efficiency of hydrogen production. The ability to store the energy

collected from solar energy units as chemical energy can be improved by making the water electrolysis reaction more efficient.

Membranes that have been coated in platinum via CVD have previously been demonstrated to be useful for hydrogen separation and storage. These materials have been shown to have a higher selectivity than that predicted by Knudsen diffusion and three orders of magnitude higher permeability of hydrogen than electroless plated platinum membrane. Further work in the field of monolayer electroplating can potentially improve the gas separation abilities of these materials, since the flux of hydrogen was found to be inversely proportional to the thickness of the platinum layer[77].

Additionally, these catalysts can be tested for their ability to improve the efficiency of other reactions, such as CO oxidation for automobile catalytic conversions. Since it has been demonstrated that noble metals like platinum and iridium can be plated onto high surface area, inexpensive supports, further research can be conducted into monolayer plating of other precious metals that are commonly used in these systems, such as rhodium or palladium.

This process can also be used to plate the exits of a carbon nanotube membrane in order to mimic the catalytic efficiency of natural enzymes. Future work involving the ability to mimic the catalytic activity of natural enzyme systems hinges on the ability to get every catalyst molecule to interact with a substrate molecule. By combining the ability to plate a monolayer of precious metals onto the surface of the charge-driven water pump, this level of catalytic efficiency can be achieved.

# References


[1] Hinds, B.J. et al, (2004) "Aligned Multiwalled Carbon Nanotube Membranes," Science, 303(62), 62-65

[2] Corry, B *J.* (2008) "Designing Carbon Nanotube Membranes for Efficient Water Desalination," Journal of Physical Chemistry 112: 1427-1434

[3] Magrez et al, (2010) "Catalytic CVD Synthesis of Carbon Nanotubes: Towards High Yield and Low Temperature Growth, Materials, 3(11): 4871-4891

[4] Tang et al (2000), "Materials Science – Single-walled 4 angstrom Carbon Nanotube Arrays," Nature 408(6808), 50-51

[5] Davis, M et al, (1988), "VPI-5: The First Molecular Sieve with Pores Larger than 10 Angstroms," Zeolites, 8: 362-366

[6] Campi, E.M, et al, (1996) "Optimization of VPI-5 Synthesis," Zeolites, 16: 15-21

[7] Ozkar, S., et al, (2009) "Intrazeolite cobalt(0) nanoclusters as low-cost and reusable catalyst for hydrogen generation from the hydrolysis of sodium borohydride," Applied Catalysis B: Environmental, 91: 21-29

[8] Maultzsch et al, (2005) "Radial Breathing Mode of Single-Walled Carbon Nanotubes: Optical Transition Energies and Chiral-index Assignment," Physical Review B, 72(15) 205438

[9] Prasad, S, (1997), "Characterization of iron infused VPI-5 Molecular Sieve," Microporous Materials, 12(1-3): 123-130

[10] Feng, Y et al, "Room Temperature Purification of Few-Walled Carbon Nanotubes with High Yield," ACS Nano 2(8):, 1634-1638

[11] Dresselhaus, M.S, et al "Raman Spectroscopy on Isolated Single Wall Carbon Nanotubes," Carbon, 40(12) 2043-2061

[12] University of Indiana Dept of Chemistry. "Standard Thermodynamic Properties of Chemical Substances." http://courses.chem.indiana.edu/c360/documents/thermodynamicdata.pdf

[13] Higman, E.B., et al, "Products from Thermal Degradation of Some Naturally Occuring Materials," Journal of Agricultrual and Food Chemistry, 18(4): 636-640.

[14] Fagerson, I.S., et al, "Thermal Degradation of Carbohydrates – A Review," Journal of Agricultural and Food Chemistry , 16(4) 747-750.

[15] Kyotani T, et al, "Preparation of Ultrafine Carbon Tubes in Nanochannels of Anodic Aluminum Oxide Film," Chemistry of Materials, 8(8): 2109-2113.

[16] Ryoo, R et al, (1999) “Synthesis of Highly Ordered Carbon Molecular Sieves via Template-Mediated Structural Transformation, The Journal of Physical Chemistry B, 103(37), 7743-7746.

[17] Iijima, S., (1991), “Helical Microtubules of GraphiticCarbon,” Nature, 354(6348): 56-58.

[18] Wang, R. Y., et al. (2010). "Ultralow-Platinum-Loading High-Performance Nanoporous Electrocatalysts with Nanoengineered Surface Structures." Advanced Materials 22(16): 1845-+.

[19] Joo, S. H., et al. (2009). "Preparation of high loading Pt nanoparticles on ordered mesoporous carbon with a controlled Pt size and its effects on oxygen reduction and methanol oxidation reactions." Electrochimica Acta 54(24): 5746-5753.

[20] Su, X., et al. (2012). "Pt monolayer deposition onto carbon nanotube mattes with high electrochemical activity." Journal of Materials Chemistry 22(16): 7979-7984.

[21] Xu, J. G. and X. W. Wang (1998). "Study of copper underpotential deposition on Au(111) surfaces." Surface Science 408(1-3): 317-325.

[22] Hou, L. X. and H. J. Qiu (2012). "Enhanced electrocatalytic performance of Pt monolayer on nanoporous PdCu alloy for oxygen reduction." Journal of Power Sources 216: 28-32.

[23] Brankovic, S.R, et al. (2001) “Metal monolayer deposition by replacement of metal adlayers on electrode surfaces.” Surface Science 474: 173-179

[24] Yagi, M, et al. (2005). “Remarkably high activity of electrodeposited IrO2 film for electrocatalytic water oxidation.” Journal of Electroanalytical Chemistry. 579: 83-88

[25] Brimaud, S. et al. (2013). “Electrodeposition of a Pt Monolayer Film: Using Kinetic Limitations for AtomicLayer Epitaxy.” Journal of the American Chemical Society 135: 11716-11719

[26] Brumlik, C.J. et al. (1994). “Templated Synthesis of Metal Microtubule Ensembles Utilizing Chemical, Electrochemical, and Vacuum Deposition Techniques.” Journal of Materials Research. 9: 1174-1183

[27] Choi, Y., et al. (2013). “Enhanced Oxygen Reduction Activity of IrCu Core Platinum Monolayer Shell Nano-electrocatalysts.” Topics in Catalysis. 56: 1059-1064

[28] Cui, X., et al. (2013). “The deposition of Au-Pt core-shell nanoparticles on reduced graphene oxide and their catalytic activity.” Nanotechnology. 24

[29] Khosaravi, M. et al (2010). “Carbon paper supported Pt/Au catalysts prepared via Cu underpotential deposition-redox replacement and investigation of their electrocatalytic activity for methanol oxidation and oxygen reduction reactions.” International Journal of Hydrogen Energy. 35: 10527-10538

[30] Koenigsmann, C. et al (2011). “Enhanced elecctrocatalytic performance of processed, ultrathin, supporeted, Pd-Pt core-shell nanowire catalysts for the oxygen reduction reaction.” Journal of the American Chemical Society. 133: 9783-9795

[31] Kye, J. et al (2013). “Platinum monolayer electrocatalyst on gold nanostructures on silicon for photoelectrochemical hydrogen evolution.” ACS Nano. 7: 6017-6023

[32] Mentus, S. et al (2004). “Electochemical water splitting on zeolite support platinum clusters.” Journal of New Materials for Electrochemical Systems. 7: 213-220

[33] Reier, T. et al (2012). “Electrocatalytic oxygen evolution reaction (OER) on Ru, Ir, and Pt catalysts: A comparitive study of nanoparticles and bulk materials.” ACS Catalysis. 2: 1765-1772

[34] Wu, Q. et al (2013). “Ultralow Pt-loading bi-metallic nanoflowers: fabrication and sensing applications.” Nanotechnology. 24

[35] Yu, Y. et al (2009). “The study of Pt@Au elecctrocatalyst based on Cu underpotential deposition and Pt redox replacement.” Electrochimica Acta. 54: 3092-3097

[36] Liu, Y. et al (2002). “Mechanism of Underpotential Deposition of Metal on Conducting Polymers.” Synthetic Metals. 126: 337-345

[37] Ghenciu, A. F. (2002). “Review of Fuel Processing Catalysts for Hydrogen Production in PEM Fuel Cell Systems.” Current Opinion in Solid State and Materials Science. 6: 389-399

[38] Grigoriev, S.A., et al (2008). “Evaluation of carbon-supported Pt and Pd nanoparticles for the hydrogen evolution reaction in PEM water electrolysers.” Journal of Power Sources. 177: 281-285

[39] Xu, J, et al (2011). “The physical-chemical properties and electrocatalytic performance of iridium oxide in oxygen evolution.” Electrochimica Acta. 56 10223-10230

[40] Omar, I.H, et al (1993). “Underpotential Deposition of Copper on Au(III) Single-crystal Surfaces – A Voltammetric and Rotating-ring-disk Electrode Study.” Journal of the Electrochemical Society. 140 (8) 2187-2192.

[41] Rouya, E, et al (2012). “Electrochemical Characterization of the Surface Area of Nanoporous Gold Films.” Journal of the Electrochemical Society. 159 (4) K97-K102

[42] Anjos, D.M., et al (2010). “Underpotential deposition of copper and silver on single crystal surfaces of rhodium.” Journal of Electroanalytical Chemistry. 639 8-14.

[43] A.A. Lucas, et al (1996) “Catalytic Synthesis of Carbon Nanotubes Using Zeolite Support,” Zeolites, 17:416-423.

[44] Tang, et al (1999), “Mono-Dispersed Single-Walled Carbon Nanotubes Formed in Channels of Zeolite Crystal: Production, Optical and Electrical Transport Properties,” Bulletin of Materials Science, 22(3): 329-333

[45] Xu, et al (2000), “Catalytic Synthesis and Characterization of Carbon Nanotubes on Unsupported and Zeolite-Supported Transition Metal Oxides Catalysts,” Acta Chimica Sinica, 58(7): 876-883

[46] Chen, J, et al (2000), “Carbon Nanotubes Synthesised in Channels of AlPO4-5 Single Crystals: First X-ray Scattering Investigations,” Solid State Communications, 116(2) 99-113.

[47] Lu, ZH, et al (2001), “Catalytic Growth of Carbon Nanotubes from the Internal Surface of Fe-loading Mesoporous Molecular Sieves Materials,” Materials Chemistry and Physics, 69(1-3): 246-251.

[48] Hwang, LP, et al (2000), “A Novel Approach to Bulk Synthesis of Carbon Nanotubes Filled with Metal by a Catalytic Chemical Vapor Deposition Method.” Chemical Physics Letters, 332(5-6): 455-460.

[49] Jacobsen, CJH, et al (2001), “Carbon Nanotube Templated Growth of Mesoporous Zeolite Single Crystals.” Chemistry of Materials, 13(12): 4416-4418.

[51] Ando, Y, et al (2004), “Controlling the Diameter Distribution of Carbon Nanotubes Grown from Camphor on a Zeolite Support,” Carbon, 43: 533-540.

[52] Jin Kim, IJ, et al (2014), “Synthesis of Verically Aligned Carbon Nanotubes on Silicate-1 Monolayer-Supported Substrate.” Journal of Nanomaterials, Article ID: 327398.

[53] Davis, ME, et al (1989), “Synthesis of VPI-5,” ACS Symposium Series, 398: 291-304.

[54] Davis, ME, et al (1989), “Physicochemical Properties of VPI-5,” Journal of the American Chemical Society, 111(11): 3919-3924.

[55] Davis, ME, et al (1990), “Crystallization of Aluminophosphate VPI-5 using Magic Angle Spinning NMR-spectroscopy,” Abstracts of Papers of the American Chemical Society, 437: 48-65.

[56] Bartomeuf, D, et al (1991), “Influence of Washing and of Heat-Treatment Conditions on the Thermal Stability of VPI-5,” Catalysis Letters, 10(3-4): 225-232.

[57] Li, B, et al (2004) “Novel Membrane and Device for Direct Contact Membrane Distillation-Based Desalination Process,” Industrial & Engineering Chemistry Research, 43(17): 5300-5309.

[58] Dresner, L, et al (1965), “Salt Concentration at Phase Boundaries in Desalination by Reverse Osmosis,” Ind. Eng. Chemical Fundamentals, 4(2): 113-118.

[59] Fang, H et al (2007), “A Charge-Driven Molecular Water Pump,” Nature Nanotechnology, 2(11): 709-712.

[60] Hinds B.J, et al, (2011), “Simulation of Steady-State Methanol Flux Through a Model Carbon Nanotube Catalyst Support,” Journal of Physical Chemistry, 11(1):

[61] Korzeniewski, C, et al (2006), “Pt Ru nanoparticle electrocatalyst with bulk alloy properties prepared through a sonichemical method,” Langnuir, 22(25): 10446-10450

[62] Burke, LD, et al (1976), “Oxygen Evolution and Corrosion at Iridium Anodes,” Journal of the Chemical Society, 72: 2431-2440

[63] Burke, LD, et al (1977), “Oxygen Evolution at Ruthenium Dioxide Anodes,” Journal of the Chemical Society, 73(11): 1659-1671

[64] Baolian, Y, et al, (2008), “Electrochemical investigation of electrocatalysts for the oxygen evolution reaction in PEM water electrolyzers,” International Journal of Hydrogen Energy, 33(19): 4955-4961

[65] Wang, Y, et al, (2009), “An Overview of Hydrogen Production Technologies,” Catalysis Today, 139(4): 244-260

[66] Wang, X, et al, (2008), “The Study of Pt@Au Electrocatalyst Based on Cu Underpotential Deposition and Pt Redox Replacement,” Electrochimica Acta. 54(11): 3092-3097

[67] Stolten, D, et al, (2013), “A Comprehensive Review on PEM Water Electrolysis,” International Journal of Hydrogen Energy, 38(12): 4901-4934

[68] Greenlee, L.F., et al., (2009) “Reverse osmosis desalination: Water sources, technology, and today's challenges” Water Research, 43(9): p. 2317-2348.

[69] Markovic, N.M., et al, (2005), “The Impact of Geometric and Surface Electronic Properties of Pt-Catalysts on the Particle Size Effect in Electrocatalysis” Journal of Physical Chemistry, 109(30): p. 14433-14440.

[70] Wilkinson, DP, et al (2006), “A Review of Anode Catalysis in the Direct Methanol Fuel Cell,” Journal of Power Sources, 155(2): 95-110.

[71] Lahiri, GK, et al (2007), “Superior Performance of a Nanostructured Platinum Catalyst in Water: Hydrogenations of Alkenes, Aldehydes, and Nitroaromatics,” Advanced Synthesis and Catalysis, 349(11-12): 1955-1962.

[72] Locke, BR, et al (2006), “Platinum Catalysed Decomposition of Hydrogen Peroxide in Aqueous-phase Pulsed Corona Electrical Discharge,” Applied Catalysis B-Environmental, 67(3-4): 149-159.

[73] Woods, R, et al (1974), “Cyclic Voltammetric Studies on Iridium Electrodes in Sulfuric Acid Solutions: Nature of Oxygen Layer and Electrode Dissolution,” Journal of Electroanalytical and Interfacial Electrochemistry, 55(3): 375-381

[74] Li, Y, et al (2006), “Copper Catalyzing Growth of Single-Walled Carbon Nanotubes on Substrates,” Nano Letters, 6(12): 2987-2990

[75] Rantell, T, et al (2002), “Multiwall Carbon Nanotubes: Synthesis and Application,” Accounts of Chemical Research, 35(12): 1008-1017

[76] Hashim, U, et al (2013), “Synthesis of Single-walled Carbon Nanotubes: Effects of Active Metals, Catalyst Supports, and Metal Loading Percentage,” Journal of Nanomaterials, Art. ID: 592464

[77] Kikuchi, E, et al (2000), “Hydrogen Permeation Properties Through Composite Membranes of Platinum Supported on Porous Alumina,” Catalysis Today, 56: 65-73

# Vita: Nicholas W. Linck

## Education

**Colorado School of Mines** – Golden, CO **B.S December 2011**
Chemistry

## Experience

***Goodrich Corporation* – Summer Internship** *(summer 2010)*

***Goodrich Corporation* – Summer Internship** *(summer 2008)*

***Colorado School of Mines* – Undergraduate Researcher** *(3 semesters)*